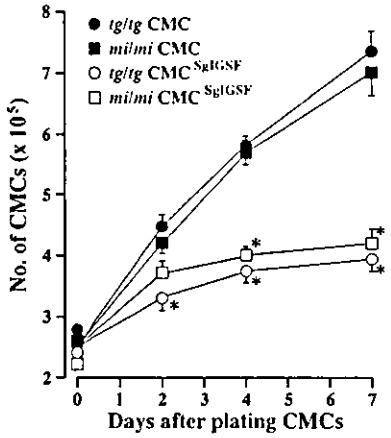

Figure 7. Growth kinetics of SgIGSF-transfected CMCs. CMCs (2.5×10^5) were suspended in 2 mL fresh medium containing PWM-SCM and plated onto 35-mm culture dishes. On the indicated days after plating, total cell numbers were counted with a standard hemocytometer. Four types of CMCs were examined: $B6^{mi/mi}$ CMCs (■), $B6^{tg/tg}$ CMCs (●), $B6^{mi/mi}$ CMCs transfected with SgIGSF cDNA (*mi/mi* CMC^{SgIGSF}; □), and $B6^{tg/tg}$ CMCs transfected with SgIGSF cDNA (*tg/tg* CMC^{SgIGSF}; ○). Mean cell numbers of triplicate samples were plotted; bars indicate SE. * $P < .01$ by Student *t* test when compared with the values of intact $B6^{mi/mi}$ or $B6^{tg/tg}$ CMCs.

$B6^{mi/mi}$ CMCs. When intact $B6^{tg/tg}$ and $B6^{mi/mi}$ CMCs were plated in fresh medium containing PWM-SCM, the total number of CMCs increased nearly 3-fold after a week (Figure 7). In contrast, there was only a 50% increase in the total cell number of $B6^{tg/tg}$ and $B6^{mi/mi}$ CMCs transfected with SgIGSF after a week (Figure 7). Cytospin preparations of $B6^{tg/tg}$ CMCs transfected with SgIGSF cDNA or with +-MITF cDNA were stained with anti-SgIGSF antibody. The plasma membranes of aggregated SgIGSF-transfected $B6^{tg/tg}$ CMCs were strongly immunoreactive to the anti-SgIGSF antibody (Figure 6C). The SgIGSF-specific fluorescence was restricted to the cell-to-cell contact areas. Although $B6^{tg/tg}$ CMCs transfected with +-MITF cDNA did not form macroscopic aggregates, microscopic aggregates of CMCs were detectable in cytospin preparations. SgIGSF-specific fluorescence was detected in the cell-to-cell contact areas of these aggregated cells, as with the $B6^{+/+}$ CMCs (compare Figures 6D and 4A). The SgIGSF-specific fluorescence was significantly stronger in SgIGSF-transfected $B6^{tg/tg}$ CMCs than in +-MITF-transfected $B6^{tg/tg}$ CMCs. The result of immunostaining of $B6^{mi/mi}$ CMCs transfected with SgIGSF cDNA was similar to that of $B6^{tg/tg}$ CMCs transfected with SgIGSF cDNA (data not shown).

Normalization of the adhesion of MITF mutant-derived CMCs to NIH/3T3 cells by transfection with SgIGSF or +-MITF

Single-cell suspension was prepared by pipetting aggregates of SgIGSF-transfected $B6^{tg/tg}$ and $B6^{mi/mi}$ CMCs. The resulting single-cell suspension of $B6^{tg/tg}$ and $B6^{mi/mi}$ CMCs transfected with SgIGSF cDNA and the single-cell suspension of $B6^{tg/tg}$ CMCs transfected with +-MITF cDNA were added to the monolayer of NIH/3T3 cells. After 3 hours' coculture, we counted the number of adhering CMCs per NIH/3T3 cell. Not only +-MITF-transfected $B6^{tg/tg}$ CMCs but also SgIGSF-transfected $B6^{tg/tg}$ and $B6^{mi/mi}$ CMCs adhered to NIH/3T3 cells as frequently as $B6^{+/+}$ CMCs (Table 2).

Transcriptional activation of the SgIGSF gene by +-MITF

We examined the effect of +-MITF and *mi*-MITF on the transcription of the SgIGSF gene, using the transient cotransfection assay. The 5′ flanking sequence of the SgIGSF gene (nt −1501 to +19 [+1 is the transcription start site]) was cloned upstream of the luciferase gene. This construct was cotransfected into MST mastocytoma cells with an empty pEF-BOS plasmid or with the vectors expressing either +-MITF or *mi*-MITF. Cotransfection with the +-MITF cDNA increased the luciferase activity 3-fold as strongly as cotransfection with the empty vector, but cotransfection with *mi*-MITF cDNA did not increase the luciferase activity (Figure 8A, upper panel). Previously we reported that +-MITF directly transactivated a number of genes by binding to CANNTG motifs.[7,17,18] The region between nt −1501 and +19 of the SgIGSF gene contained 2 CANNTG motifs: CATTTG (nt −1490 to −1485) and CACTTG (nt −682 to −677). We mutated the CATTTG (nt −1490 to −1485) motif to C*T*TTAG and found that the mutation abolished the transactivation effect of +-MITF (Figure 8A, upper panel). Next we deleted the CATTTG (nt −1490 to −1485) motif from the SgIGSF promoter. The resulting shorter luciferase construct, which contained only the CACTTG (nt −682 to −677) motif, was not transactivated by cotransfection with the +-MITF cDNA (Figure 8A, upper panel). We performed similar luciferase assays using Jurkat lymphoid cells instead of MST cells. Neither +-MITF nor *mi*-MITF produced any transactivation effects on the 3 luciferase constructs (Figure 8A, lower panel).We examined in vitro binding of +-MITF to the CATTTG motif by EGMSA. Two oligonucleotides containing the CATTTG (nt −1490 to −1485; oligonucleotide E) and mutated (C*T*TTAG; oligonucleotide mE) motifs were synthesized. When oligonucleotide E was incubated with the GST–+-MITF fusion protein, a slowly migrating band was detected (Figure 8B, lane 2). The band appeared to be due to the specific binding of oligonucleotide E to +-MITF but not to GST, because incubation of this oligonucleotide with the GST protein alone did not yield any bands (Figure 8B, lane 1). To examine whether the binding between oligonucleotide E and GST–+-MITF was dependent on the CATTTG motif, the binding reaction was performed in the presence of an excess amount of unlabeled competitors. The binding of labeled oligonucleotide E to GST–+-MITF was completely canceled out by adding an excess amount of unlabeled oligonucleotide E, but not by adding the same amount of unlabeled oligonucleotide mE (Figure 8B, lanes 3 and 4).

Discussion

In the present study, we examined cell-to-cell adhesion phenotypes of CMCs derived from 3 types of MITF mutant mice, $B6^{tg/tg}$, $B6^{mi/mi}$, and $B6^{Miwh/Miwh}$. The *mi* and Mi^{wh} mutant alleles encode MITFs with deletion (*mi*-MITF)[1,3,4] and alteration (Mi^{wh}-MITF),[23] respectively, of a single amino acid at the basic domain,[4] whereas *tg* is a null mutation.[1,9,10] The *mi*-MITF has a significant inhibitory effect on transcription of various genes.[8,13,19] The Mi^{wh}-MITF has a decreased but detectable transcription activity on some genes and an inhibitory effect on other genes.[23,33] Although these mutant alleles have different structural and functional abnormalities, poor

Table 2. Normalization of attachment of $B6^{tg/tg}$ and $B6^{mi/mi}$ CMCs to NIH/3T3 fibroblasts by transfection with SgIGSF or ± MITF cDNA

CMCs	No. of adhering CMCs per NIH/3T3 cell*
+/+ CMCs	0.163 ± 0.006
tg/tg CMCs	0.053 ± 0.006†
tg/tg CMCs transfected with SgIGSF	0.189 ± 0.026
tg/tg CMCs transfected with +-MITF	0.169 ± 0.017
tg/tg CMCs transfected with vector	0.057 ± 0.005†
mi/mi CMCs	0.045 ± 0.005†
mi/mi CMCs transfected with SgIGSF	0.156 ± 0.029

*Mean ± SE of 3 dishes.
†$P < .01$ by Student *t* test when compared with the values of $B6^{+/+}$ CMCs.

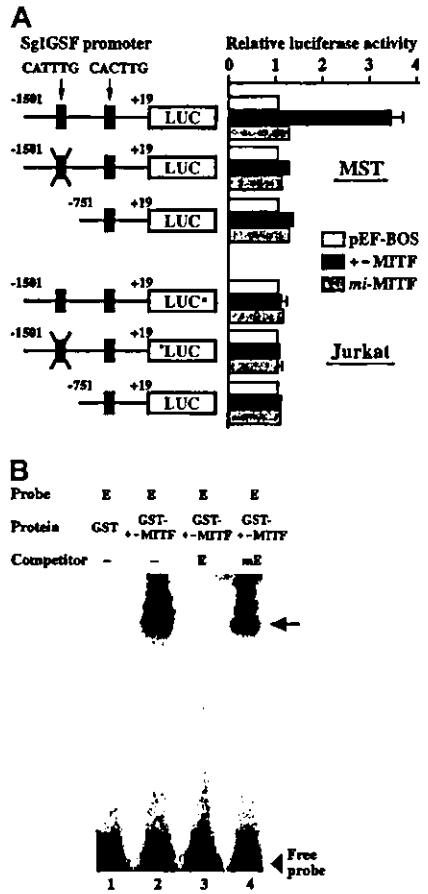

Figure 8. Luciferase assay and EGMSA. (A) Transactivation of the SgIGSF promoter by +-MITF. The promoter sequences of the SgIGSF from −1501 to +19 were inserted upstream of the luciferase (LUC) gene of the pSPLuc vector. In one construct, the CATTTG motif in the promoter was mutated to C*TTAG (indicated by X). The deletion construct lacking the CATTTG motif was also made. These reporter constructs were cotransfected into MST (upper panel) or Jurkat (lower panel) cells with the empty pEF-BOS vector or the vector containing either +-MITF or *mi*-MITF cDNA. Mean values of the luciferase activity obtained with triplicate samples were plotted; bars indicate SE. In most cases, the SE values were too small to be shown by bars. (B) In vitro binding between the CATTTG motif and +-MITF. Oligonucleotide E was labeled with α-^{32}P dCTP and used as a probe. The unlabeled oligonucleotides E and mE were used as competitors. The probe was incubated with either GST or GST–+-MITF protein in the absence (−) or presence of an excess amount of either competitor. An arrow indicates a protein-DNA complex.

adhesion of CMCs to NIH/3T3 fibroblasts was common among CMCs derived from all 3 MITF mutant mice.

By screening the (+/+ − *mi/mi*) subtracted cDNA library, we identified SgIGSF as a transcriptionally down-regulated gene in B6$^{mi/mi}$ CMCs. SgIGSF is a member of the immunoglobulin superfamily that was recently cloned from the cDNA library of adult mouse testes. Wakayama et al[24] showed that SgIGSF was preferentially expressed by spermatogenic cells and suggested that SgIGSF may participate in the interaction of spermatogenic cells with Sertoli cells. Expression of SgIGSF was readily detectable in B6$^{+/+}$ CMCs, but not in CMCs derived from 3 types of MITF mutant mice examined.

A human homolog of SgIGSF is known as IGSF4 (immunoglobulin superfamily number 4)[34]: there is 98% identity between the 2 molecules at amino acid levels. Both SgIGSF and IGSF4 have an extracellular domain with significant homology to neural cell adhesion molecule 1 (NCAM-1) and NCAM-2.[24] A putative motif sequence that connects to actin cytoskeleton was present in the intracellular domain of SgIGSF and IGSF4.[35] Recently, IGSF4 was found to be identical to tumor suppressor in lung cancer 1 (TSLC1).[36,37] TSLC1 was originally cloned from the genomic region that frequently exhibits loss of heterozygosity in human lung cancers and possesses tumor-suppressor activity. A recent study by Masuda et al[38] showed that TSLC1/IGSF4 localized to the plasma membrane in cell-to-cell contact areas and that cells overexpressing TSLC1/IGSF4 more frequently formed aggregates. SgIGSF as well as TSLC1/IGSF4 appeared to mediate intercellular adhesion.

Immunofluorescence analysis of cytospin preparations showed that the subcellular localization of SgIGSF was restricted to cell-to-cell contact areas among B6$^{+/+}$ CMCs. This localization pattern was common not only to TSLC1/IGSF4[38] but also to well-characterized intercellular adhesion molecules, such as E-cadherin and nectins.[39,40] In B6$^{+/+}$ CMCs adhering to NIH/3T3 fibroblasts, SgIGSF was located primarily in the lamellipodial structure, where cytoskeletal components and regulators, such as vinculin and Rac-1, are known to accumulate in mast cells.[41] These results suggested that SgIGSF may mediate adhesion either among CMCs or between CMCs and NIH/3T3 fibroblasts.

Consistent with the results of immunofluorescence, overexpression of SgIGSF in B6$^{tg/tg}$ and B6$^{mi/mi}$ CMCs resulted in the formation of macroscopic aggregates in suspension culture, although intact B6$^{tg/tg}$ and B6$^{mi/mi}$ CMCs did not form such aggregates. SgIGSF appeared to function as a homophilic adhesion molecule. However, this homophilic interaction may take place only when SgIGSF is overexpressed. In fact, B6$^{+/+}$ CMCs did not form such macroscopic aggregates. B6$^{tg/tg}$ and B6$^{mi/mi}$ CMCs overexpressing SgIGSF adhered to NIH/3T3 fibroblasts as well as B6$^{+/+}$ CMCs, although original B6$^{tg/tg}$ and B6$^{mi/mi}$ CMCs did not. This indicates that SgIGSF is necessary for adhesion of CMCs to NIH/3T3 fibroblasts. Because NIH/3T3 fibroblasts did not express SgIGSF, SgIGSF appeared to serve as a heterophilic adhesion molecule in the interaction between CMCs and NIH/3T3 fibroblasts. The counterpart of SgIGSF that is expressed by NIH/3T3 fibroblasts remains to be identified. Probably the heterophilic interaction may be more physiological than the homophilic interaction, because the overexpression of SgIGSF was not necessary for the heterophilic interaction.

Expression levels of the SgIGSF protein were not reduced in CMCs derived from WB$^{W/W}$ and WBB6F$_1$$^{W/W^v}$ mice. The *W* allele encodes the mutant KIT without the extracellular domain,[42] and the *W^v* allele encodes the mutant KIT with an intact extracellular domain and a mutated tyrosine kinase domain.[43] In the coculture with NIH/3T3 fibroblasts, WBB6F$_1$$^{W/W^v}$ CMCs normally adhered to NIH/3T3 fibroblasts, whereas WB$^{W/W}$ CMCs did not.[44] Because WB$^{W/W}$ CMCs expressed SgIGSF, their deficient adhesion to NIH/3T3 fibroblasts was attributable to the deficient expression of the extracellular domain of KIT. On the other hand, B6$^{mi/mi}$, B6$^{tg/tg}$, and B6$^{Miwh/Miwh}$ CMCs did not adhere to NIH/3T3 fibroblasts. Although B6$^{mi/mi}$ and B6$^{tg/tg}$ CMCs showed deficient expression of KIT,[8] B6$^{Miwh/Miwh}$ CMCs did show normal expression levels of KIT.[23] Therefore, the deficient adhesion of CMCs of MITF mutants was attributable to the deficient expression of SgIGSF. Both KIT and SgIGSF appeared necessary for adhesion of CMCs to NIH/3T3 fibroblasts.

Defective expression of SgIGSF in CMCs derived from all MITF mutant mice suggested that the presence of +-MITF was essential for the expression of SgIGSF in mast cells. However, +-MITF did not appear necessary for the expression of SgIGSF in cells other than mast cells. In fact, the expression of SgIGSF was comparable between testes, spleens, lungs, and stomachs of B6$^{+/+}$ and B6$^{tg/tg}$ mice. Probably, other transcription factors may compensate for +-MITF in these tissues. The transactivation effect of +-MITF on the SgIGSF gene promoter was detected in MST

mastocytoma cells but not in Jurkat lymphoid cells. In addition, transfection with the +-MITF cDNA normalized the expression of SgIGSF in $B6^{lg/lg}$ CMCs. The transactivation of +-MITF was mediated through CATTTG motif (nt −1490 to −1485) in the promoter region of the SgIGSF gene, at least in mast cells.

In summary, we identified a new mast cell adhesion molecule, SgIGSF. Transcription of the SgIGSF gene was critically regulated by +-MITF in mast cells. SgIGSF appeared to mediate not only the aggregation of CMCs through its homophilic interaction, but also the adhesion of CMCs to NIH/3T3 fibroblasts through its heterophilic interaction.

Acknowledgments

We thank J. D. Esko for MST cells, H. Arnheiter for VGA-$9^{lg/lg}$ mice, S. Nagata for pEF-BOS, and T. Akagi for pCX4bsr. We also thank M. Kohara, T. Sawamura, and K. Hashimoto for technical assistance.

References

1. Hodgkinson CA, Moore KJ, Nakayama A, et al. Mutations at the mouse microphthalmia locus are associated with defects in a gene encoding a novel basic-helix-loop-helix-zipper protein. Cell. 1993;74:395-404.
2. Hughes JJ, Lingrel JB, Krakowsky JM, Anderson KP. A helix-loop-helix transcription factor-like gene is located at the *mi* locus. J Biol Chem. 1993;268:20687-20690.
3. Hemesath TJ, Steingrimsson E, McGill G, et al. Microphthalmia, a critical factor in melanocyte development, defines a discrete transcription factor family. Genes Dev. 1994;8:2770-2780.
4. Steingrimsson E, Moore KJ, Lamoreux ML, et al. Molecular basis of mouse microphthalmia (*mi*) mutations helps explain their developmental and phenotypic consequences. Nat Genet. 1994;8: 256-263.
5. Morii E, Takebayashi K, Motohashi H, et al. Loss of DNA binding ability of the transcription factor encoded by the mutant *mi* locus. Biochem Biophys Res Commun. 1994;205:1299-1304.
6. Takebayashi K, Chida K, Tsukamoto I, et al. Recessive phenotype displayed by a dominant negative microphthalmia-associated transcription factor mutant is a result of impaired nuclear localization potential. Mol Cell Biol. 1996;16:1203-1211.
7. Ito A, Morii E, Maeyama E, et al. Systematic method to obtain novel genes that are regulated by *mi* transcription factor (MITF): impaired expression of granzyme B and tryptophan hydroxylase in *mi/mi* cultured mast cells. Blood. 1998;91: 3210-3221.
8. Ito A, Morii E, Kim D-K, et al. Inhibitory effect of the transcription factor encoded by the *mi* mutant allele in cultured mast cells of mice. Blood. 1999; 93:1189-1196.
9. Tachibana M, Hara Y, Vyas D, et al. Cochlear disorder associated with melanocyte anomaly in mice with a transgenic insertional mutation. Mol Cell Neurosci. 1992;3:433-445.
10. Tsujimura T, Hashimoto K, Morii E, et al. Involvement of transcription factor encoded by the mouse *mi* locus (MITF) in apoptosis of cultured mast cells induced by removal of interleukin-3. Am J Pathol. 1997;151:1043-1051.
11. Silvers WK. The Coat Colors of Mice: A Model for Mammalian Gene Action and Interaction. New York, NY: Springer-Verlag; 1979.
12. Steingrimsson E, Tessarollo L, Pathak B, et al. Mitf and Tfe3, two members of the Mitf-Tfe family of bHLH-Zip transcription factors, have important but functionally redundant roles in osteoclast development. Proc Natl Acad Sci U S A. 2002;99: 4477-4482.
13. Morii E, Ogihara H, Oboki K, et al. Inhibitory effect of the *mi* transcription factor encoded by the mutant *mi* allele on GA binding protein-mediated transcript expression in mouse mast cells. Blood. 2001;97:3032-3039.
14. Kasugai T, Oguri K, Jippo-Kanemoto T, et al. Deficient differentiation of mast cells in the skin of *mi/mi* mice: usefulness of in situ hybridization for evaluation of mast cell phenotype. Am J Pathol. 1993;143:1337-1347.
15. Ge Y, Jippo T, Lee Y-M, Adachi S, Kitamura Y. Independent influence of strain difference and *mi* transcription factor on the expression of mouse mast cell chymases. Am J Pathol. 2001;158:281-292.
16. Jippo T, Lee Y-M, Katsu Y, et al. Deficient transcription of mouse mast cell protease 4 gene in mutant mice of *mi/mi* genotype. Blood. 1999;93:1942-1950.
17. Morii E, Jippo T, Tsujimura T, et al. Abnormal expression of mouse mast cell protease 5 gene in cultured mast cells derived from mutant *mi/mi* mice. Blood. 1997;90:3057-3066.
18. Morii E, Tsujimura T, Jippo T, et al. Regulation of mouse mast cell protease 6 gene expression by transcription factor encoded by the *mi* locus. Blood. 1996;88:2488-2494.
19. Tsujimura T, Morii E, Nozaki M, et al. Involvement of transcription factor encoded by the *mi* locus in the expression of *c-kit* receptor tyrosine kinase in cultured mast cells of mice. Blood. 1996;88:1225-1233.
20. Ebi Y, Kanakura Y, Jippo-Kanemoto T, et al. Low *c-kit* expression of cultured mast cells of *mi/mi* genotype may be involved in their defective responses to fibroblasts that express the ligand for *c-kit*. Blood. 1992;80:1454-1462.
21. Fujita J, Nakayama H, Onoue H, et al. Failure of *W/W^v* mouse-derived cultured mast cells to enter S phase upon contact with NIH/3T3 fibroblasts. Blood. 1988;72:463-468.
22. Fujita J, Nakayama H, Onoue H, et al. Fibroblast-dependent growth of mouse mast cells *in vitro*: duplication of mast cell depletion in mutant mice of *W/W^v* genotype. J Cell Physiol. 1988;134:78-84.
23. Kim D-K, Morii E, Ogihara H, et al. Different effect of various mutant MITF encoded by *mi*, *MP^t*, or *M^{wh}* allele on phenotype of murine mast cells. Blood. 1999;93:4179-4186.
24. Wakayama T, Ohashi K, Mizuno K, Iseki S. Cloning and characterization of a novel mouse immunoglobulin superfamily gene expressed in early spermatogenic cells. Mol Reprod Dev. 2001;60: 158-164.
25. Nakahata T, Spicer S, Cantey JR, Ogawa M. Clonal assay of mouse mast cell colonies in methylcellulose culture. Blood. 1982;60:352-362.
26. Montgomery RI, Lidholt K, Flay NW, Vertel B, Lindahl U, Esko JD. Stable heparin-producing cell lines derived from the Furth murine mstocytoma. Proc Natl Acad Sci U S A. 1992;89:11327-11331.
27. Ito A, Kataoka TR, Watanabe M, et al. A truncated isoform of the PP2A B56 subunit promotes cell motility through paxillin phosphorylation. EMBO J. 2000;19:562-571.
28. Morii E, Oboki K, Kataoka TR, Igarashi K, Kitamura Y. Interaction and cooperation of *mi* transcription factor (MITF) and Myc-associated Zinc-finger protein-related factor (MAZR) for transcription of mouse mast cell protease 6 gene. J Biol Chem. 2002;277:8566-8571.
29. Fujii T, Tamura K, Masai K, Tanaka H, Nishimune Y, Nojima H. Use of stepwise subtraction to comprehensively isolate mouse genes whose transcription is up-regulated during spermatogenesis. EMBO Rep. 2002;3:367-372.
30. Oboki K, Morii E, Kataoka TR, Jippo T, Kitamura Y. Isoforms of *mi* transcription factor preferentially expressed in cultured mast cells of mice. Biochem Biophys Res Commun. 2002;290:1250-1254.
31. Akagi T, Shishido T, Murata K, Hanafusa H. v-Crk activates the phosphoinositide 3-kinase/AKT pathway in transformation. Proc Natl Acad Sci U S A. 2000;97:7290-7295.
32. Mizushima S, Nagata S. pEF-BOS, a powerful mammalian expression vector. Nucleic Acids Res. 1990;18:5322.
33. Kataoka TR, Morii E, Oboki K, et al. Dual abnormal effects of mutant MITF encoded by Miwh allele on mouse mast cells: decreased but recognizable transactivation and inhibition of transactivation. Biochem Biophys Res Commun. 2002;297:111-115.
34. Gomyo H, Arai Y, Tanigami A, et al. A 2-Mb sequence-ready contig map and a novel immunoglobulin superfamily gene IGSF4 in the LOH region of chromosome 11q23.2. Genomics. 1999; 62:139-146.
35. Fukuhara H, Kuramochi M, Nobukuni T, et al. Isolation of the TSLL1 and TSLL2 genes, members of the tumor suppressor TSLC1 gene family encoding transmembrane proteins. Oncogene. 2001;20:5401-5407.
36. Kuramochi M, Fukuhara H, Nobukuni T, et al. TSLC1 is a tumor suppressor gene in human non-small-cell lung cancer. Nat Genet. 2001;27: 427-430.
37. Pletcher MT, Nobukuni T, Fukuhara H, et al. Identification of tumor suppressor candidate genes by physical and sequence mapping of the TSLC1 region of human chromosome 11q23. Gene. 2001;273:181-189.
38. Masuda M, Yageta M, Fukuhara H, Kuramochi M, Maruyama T, Nomoto A, Murakami Y. The tumor suppressor protein TSLC1 is involved in cell-cell adhesion. J Biol Chem. 2002;277:31014-31019.
39. Takahasi K, Nakanishi H, Miyahara M, et al. Nectin/PRR: an immunoglobulin-like cell adhesion molecule recruited to cadherin-based adherens junctions through interaction with Afadin, a PDZ domain-containing protein. J Cell Biol. 1991;145: 539-549.
40. Miyahara M, Nakanishi H, Takahashi K, Satoh-Horikawa K, Tachibana K, Takai Y. Interaction of nectin with afadin is necessary for its clustering at cell-cell contact sites but not for its cis dimerization or trans interaction. J Biol Chem. 2000;275: 613-618.
41. Guillemot J-C, Montcourrier P, Vivier E, Davoust J, Chavrier P. Selective control of membrane ruffling and actin plaque assembly by the Rho GTPases Rac1 and CDC42 in FcεRI-activated rat basophilic leukemia (RBL-2H3) cells. J Cell Sci. 1997;110:2215-2225.
42. Hayashi S, Kunisada T, Ogawa M, Yamaguchi K, Nishikawa S. Exon skipping by mutation of an authentic splice site of *c-kit* gene in *W/W* mouse. Nucleic Acids Res. 1991;19:1267-1271.
43. Nocka K, Tan JC, Chiu E, et al. Molecular bases of dominant negative and loss of function mutations at the murine c-kit/white spotting locus: W^{37}, W^v, W^{41} and W. EMBO J. 1990;9:1805-1813.
44. Adachi S, Ebi Y, Nishikawa S, et al. Necessity of extracellular domain of *W* (*c-kit*) receptors for attachment of murine cultured mast cells to fibroblasts. Blood. 1992;78:650-656.

Mammalian Mcm2/4/6/7 complex forms a toroidal structure

Norikazu Yabuta[1,†], Naoko Kajimura[2,†], Kouta Mayanagi[2], Michio Sato[3], Takahito Gotow[4], Yasuo Uchiyama[4], Yukio Ishimi[3] and Hiroshi Nojima[1,*]

[1]*Department of Molecular Genetics, Research Institute for Microbial Diseases, Osaka University, 3-1 Yamadaoka;* [4]*Department of Cell Biology and Neurosciences (A1), Osaka University Graduate School of Medicine, 3-4 Yamadaoka, Suita, Osaka 565-0871, Japan*

[2]*Biomolecular Engineering Research Institute, 6-2-3 Furuedai, Suita, Osaka 565-0874, Japan*

[3]*Mitsubishi Kagaku Institute of Life Sciences, 11 Minamiooya, Machida, Tokyo 194-8511, Japan*

Abstract

***Background*: The Mcm proteins are a family of six homologous proteins (Mcm2–7) that play an important role in DNA replication. They form Mcm4/6/7 and Mcm2/4/6/7 complexes, but their structures are not known.**

***Results*: We found that the human Mcm2/4/6/7 tetramer forms a toroidal structure, with a central cavity about 3–4 nm in diameter. Observations were made using electron microscopy, employing the image analysis of single particles. The most predominant averaged image displayed a toroid harbouring four bulges forming corners, one of which was larger than the others. This structure was very similar to the mouse Mcm2/4/6/7 tetramer that was independently prepared and analysed by electron microscopy. These toroidal structures are distinct from that of the Mcm4/6/7 hexamer, which was also examined by electron microscopy. GST(glutathione S-transferase)-pull down and two hybrid experiments suggest that a putative Mcm6-Mcm6 hinge contributes to the formation of the Mcm7/4/6/6/4/7 heterohexamer.**

***Conclusions*: The Mcm2/4/6/7 tetramer forms a toroidal structure that is distinct from that of the Mcm4/6/7 hexamer in size and shape.**

Introduction

The Mcm protein family consists of six homologous proteins (Mcm2–7) which form a hexameric complex that plays a pivotal role in the initiation of DNA replication (Lee & Bell 2000; Lei & Tye 2001; Nishitani & Lygerou 2002). The six Mcm proteins are present in almost equivalent amounts in soluble cell extracts and on chromatin, where they form a heterohexameric complex (Fujita *et al.* 1997; Crevel *et al.* 2001). This complex can easily break down into subcomplexes containing Mcm4, 6 and 7 (600 kDa), Mcm2, 4, 6 and 7 (450 kDa), or Mcm3 and 5 (Ishimi 1997; Lee & Hurwitz 2000; Prokhorova & Blow 2000).

All six Mcm proteins belong to the AAA^+ superfamily of ATPases (Ogura & Wilkinson 2001). These ATPases are characterized by conserved motifs in a central domain that are known to be required for viability *in vivo* and coordinated ATP hydrolysis *in vitro* (Schwacha & Bell 2001). It has been shown that mammalian Mcm4, 6 and 7 form a hexamer consisting of two molecules of each protein, that functions as a DNA helicase (Ishimi 1997; You *et al.* 1999). In contrast, the Mcm2/4/6/7 complex does not have DNA helicase activity (Ishimi 1997). Moreover, the addition of purified Mcm2 to the Mcm4/6/7 complex abolishes its DNA helicase activity (Ishimi *et al.* 1998). This is achieved by binding of the carboxyl-half of Mcm2 to Mcm4, which serves to disassemble the Mcm4/6/7 hexamer (Ishimi *et al.* 2001). The phosphorylation of Mcm4 by cyclin A/Cdk2 also acts to inhibit the helicase activity of the Mcm4/6/7 complex (Ishimi *et al.* 2000). Examination of the yeast Mcm4/6/7 complex shows that these three proteins form the catalytic core of the helicase, while Mcm2 and Mcm3 and 5 may be involved in regulating the activity of this complex (Lee & Hurwitz 2000; Sato *et al.* 2000; Schwacha & Bell 2001).

A number of DNA helicases that have been isolated from both prokaryotes and eukaryotes function as hexamers and they form ring structures when visualized by electron microscopy (Hingorani & O'Donnell 2000). Previously we reported that the Mcm4/6/7 hexameric subcomplex also appears as a ring structure in electron microscope analysis (Sato *et al.* 2000). In this paper, we report that the Mcm2/4/6/7 complex also forms a toroidal structure

Communicated by: Fumio Hanaoka

**Correspondence*: E-mail: hnojima@biken.osaka-u.ac.jp

†These two authors contributed equally to this work.

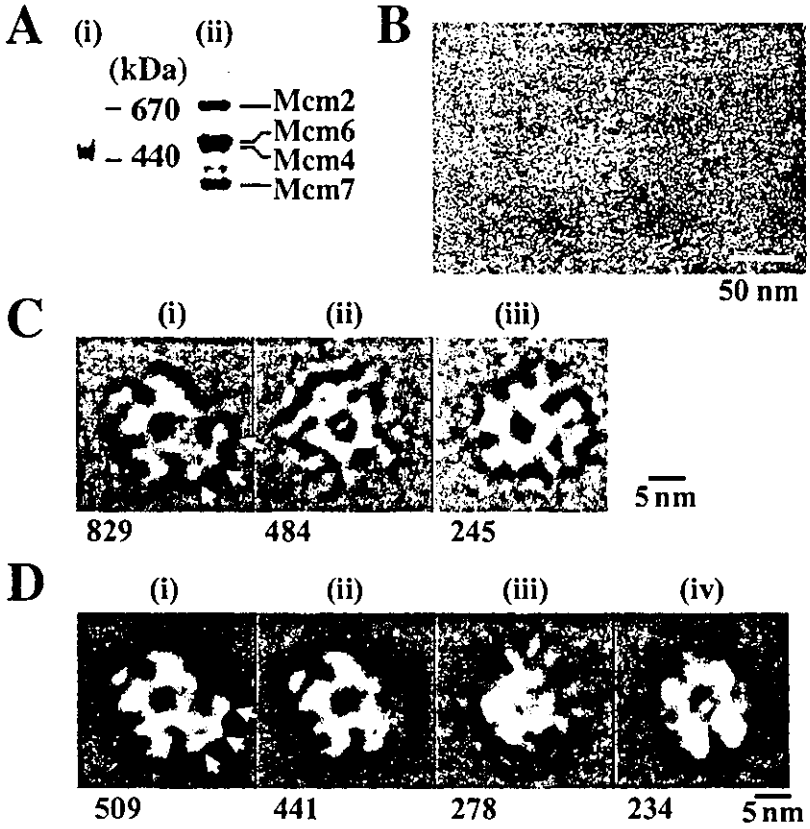

Figure 1 Electron microscopy of human and mouse Mcm2/4/6/7 complexes. (A) The 450 kDa Mcm2/4/6/7 complex was purified from HeLa cells and subjected to native PAGE (i) and SDS-PAGE (ii) analyses to show the homogeneity of the complex. (B) Representative electron micrograph of a negatively stained human Mcm2/4/6/7 complex. Bar = 50 nm. (C) Class averages of the human Mcm2/4/6/7 tetramers obtained by multivariate statistical analysis (MSA) and subsequent hierarchic ascendant classification (HAC) of 1558 images. Numbers below each class average represent the frequency of images used to obtain the averaged image. (D) Class averages of the mouse Mcm2/4/6/7 tetramer obtained by MSA and HAC using 1462 images. The numbers below each figure represent the frequency of images used to obtain the averaged image. One of the bulges of the most frequently occurring class average (C-i and D-i) is larger than the others and harbours three sharp density peaks (indicated by arrows). Bar = 5 nm.

with a ring shape that is distinct from the Mcm4/6/7 complex structure. We also examined the association of each component in the Mcm2/4/6/7 complex by two-hybrid analysis and GST-pull down experiments. These observations suggest that Mcm6 may play a central role in the formation of the Mcm4/6/7 hexameric complex.

Results

Electron microscopy and image analysis of the Mcm2/4/6/7 tetramer

We purified the Mcm2/4/6/7 complex from HeLa cells for examination by electron microscopy. The purity of this preparation was confirmed by native polyacrylamide gel electrophoresis (PAGE) (Fig. 1A-i). We also confirmed the purity of each component by SDS-PAGE (Fig. 1A-ii). The bands for each Mcm protein were of an almost equivalent intensity, which indicates that the complex consists of equal amounts of the Mcm2, 4, 6 and 7 proteins. Each Mcm protein is around 100 kDa in size, while the Mcm2/4/6/7 complex from HeLa cells is about 450 kDa. This suggests that the Mcm2, 4, 6 and 7 proteins assemble into a heterotetramer. The assembly of Mcm2, 4, 6 and 7 proteins into the heterotetramer was also suggested by glycerol gradient centrifugation (Ishimi 1997).

Figure 1B shows the typical electron micrograph of a negatively stained Mcm2/4/6/7 complex. The Mcm2/4/6/7 complex images showed that the particles were roughly homogeneous in size, but heterogeneous in shape. To analyse the variability of the particle shapes, a multivariate statistical analysis (MSA) and subsequent hierarchic ascendant classification (HAC) (van Heel *et al.* 1996) was applied to all particles about 15 nm in diameter (n = 1558). This analysis revealed that the particle images could be classified into three major groups that contained 829, 484 and 245 images, respectively (Fig. 1C). They all showed a toroidal structure with a central hole 3–4 nm in diameter, which is sufficiently wide to allow double-stranded DNA to pass through. The most frequent image (Fig. 1C-i) is an asymmetrical toroidal structure 15 nm × 18 nm in size harbouring four bulges forming corners, one of which is larger than the others. These bulges probably correspond to each of the four Mcm proteins making up this complex. It is notable that one of the bulges is larger than the others and harbours three sharp density peaks (indicated by arrows). This is probably the reason for the asymmetrical shape of the complex.

This larger region may correspond to Mcm2, as it has the largest molecular weight of the four proteins. The other images also display toroidal structures with complicated protruding structures of distinct size and shape (Fig. 1C-ii and -iii). The significance of these structures is currently unknown.

To assess whether the ring-shaped images of the Mcm2/4/6/7 tetramer are also visualized when Mcm proteins from other species make up the complex, we analysed the structure of the mouse Mcm2/4/6/7 complex with the same method. The mouse complex was prepared from insect cells that had been co-infected with a recombinant baculovirus bearing the mouse *MCM2, 4, 6* and 7 genes. As shown in Fig. 1D, MSA and HAC of 1462 randomly selected images resulted in the classification of these images into four major groups that contained 509, 441, 278 and 234 images, respectively. The averaged image of the most frequently occurring group (Fig. 1D-i) is very similar to the human Mcm2/4/6/7 complex in both shape and size as it has an arm that harbours three extra regions with high electron density (denoted by arrows). Thus, the averaged image we present in Fig. 1C-i is reproducible and reliable. The second most frequently occurring image of the mouse complex (Fig. 1D-ii) also shows a similar toroidal shape, but it lacks the three extra regions. This suggests that these regions are fragile. The rest of the averaged images (Fig. 1D-iii,vi) display pseudo-toroids. One of these displays a horseshoe-like structure, the significance of which remains unclear.

Electron microscopy, using a rotary shadowing technique, of the human Mcm2/4/6/7 tetramer revealed similar toroidal shapes (data not shown). This further confirms the toroidal structure of this tetramer.

Electron microscopy and image analysis of the Mcm4/6/7 hexamer

We previously reported the raw images of the human Mcm4/6/7 complex obtained by electron microscopy using negative staining (Sato *et al.* 2000). To more precisely compare the size and shape of this complex with the Mcm2/4/6/7 tetramer reported here, we prepared the Mcm4/6/7 complex from HeLa cells and again analysed its structure by electron microscopy and image analysis. The purity of the complex (Fig. 2A-i) and its components (Fig. 2A-ii) was confirmed by PAGE. Before the experiments, we also confirmed that the Mcm4/6/7 complex has the same ATPase and helicase activity as previously described (Ishimi 1997).

As demonstrated in a representative electron micrograph (Fig. 2B), two kinds of particles could be observed: one apparently showing a central channel (depicted by arrows) and the other showing a central slit (depicted by arrowheads). These data are basically consistent with those obtained in our previous study (Sato *et al.* 2000). We applied a reference-free alignment method to each image to obtain two types of averaged image. The averaged image obtained from the channel-bearing particles (Fig. 2C-i) revealed a toroidal structure 13–14 nm in diameter. The diameter of the central channel was 3–4 nm, which is sufficiently wide for DNA to pass through. It is of note is that six bulges were observed at the outer region of the complex, which might correspond to each of the six Mcm proteins making up the complex, and that one of these bulges is split into two (denoted by an arrow in Fig. 2C-i). The split bulge may represent the staggered structure of the neighbouring Mcm proteins that has also been observed in the hexameric ring of the replicative helicase-primase of bacteriophage T7 (Sawaya *et al.* 1999). The other averaged image of the Mcm4/6/7 complex (Fig. 2C-ii) was obtained from the slit-bearing particles and shows a symmetrical structure displaying four regions with a high density that are separated by a central slit and a small bulge at one end of the image (denoted by an arrow). This image may represent a side view of the Mcm4/6/7 complex.

To confirm the reproducibility of this toroidal structure, we prepared mouse Mcm4/6/7 complexes from insect cells co-infected with a recombinant baculovirus bearing the mouse *MCM4, 6* and 7 genes and observed them by electron microscopy. The averaged toroidal image was similar to the human Mcm4/6/7 complex in both shape and size, indicating that the averaged image in Fig. 2C is reproducible. The toroids display six almost symmetrical petals plus an extra outer bulge between the two symmetrical bulges (denoted by an arrow in Fig. 2D). This may also reflect the staggered structure of the neighbouring Mcm proteins as described above.

GST-pull down assay

To explore in detail the Mcm–Mcm interactions that are required to form the toroidal structures of the Mcm4/6/7 hexamer and the Mcm2/4/6/7 tetramer, we examined the interaction between Mcm proteins *in vitro*. For this purpose, Mcm2, 4, 6 and 7 proteins were expressed as GST fusion proteins in bacteria and were bound to glutathione-Sepharose beads. These fusion proteins were subjected to SDS-PAGE and stained with Coomassie Blue to assess the purity and quantity of each protein (Fig. 3A). We used bacterial lysates that express recombinant human Mcm protein for the pull-down assay because the bacterial cells lack Mcm homologues, which allows an examination of the direct interaction

between human Mcm-Mcm proteins without the influence of the Mcm homologue in the lysate. Bacterial lysates expressing FLAG-tagged Mcm2, 6 or 7 were mixed and incubated with the GST-tagged Mcm2, 4, 6 or 7 fusion proteins bound to glutathione-Sepharose beads. After precipitation of the beads by centrifugation and washing twice with buffer, the proteins retained in the beads were analysed by Western blotting with anti-FLAG antibody (Fig. 3B).

FLAG-Mcm2 was equally well co-precipitated by GST-tagged Mcm4, 6 and 7, but not by GST-tagged Mcm2 or GST alone, as judged by the intensity of the bands (Fig. 3B, top panel). FLAG-Mcm6 was equally co-precipitated with GST-tagged Mcm2, 4 and 6 but not with GST-Mcm7 (Fig. 3B, middle panel). The intensity of the band between FLAG-Mcm7 and GST-Mcm4 was stronger than those between FLAG-Mcm7 and GST-Mcm2, 6 or 7, suggesting that the Mcm7–Mcm4 interaction is stronger than the Mcm7–Mcm2, Mcm7–Mcm6 and Mcm7–Mcm7 interactions (Fig. 3B, bottom panel). The weak band between FLAG-Mcm7 with GST-Mcm6 further confirms the weak interaction between Mcm7–Mcm6 described above.

Unlike the other FLAG-Mcms, a small amount of FLAG-Mcm4 was already co-precipitating with GST alone, indicating that FLAG-Mcm4 could be nonspecifically bound to Sepharose (data not shown). Therefore, we could not determine whether FLAG-Mcm4 interacts with GST-Mcm4.

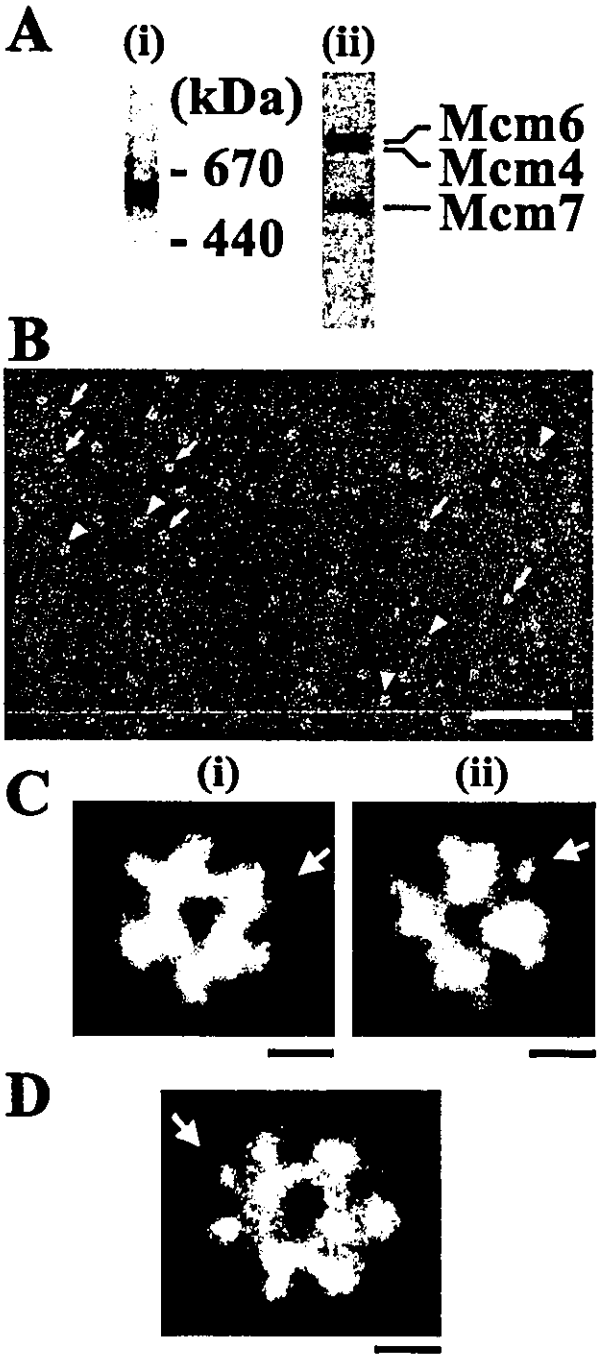

Figure 2 Electron microscope observation of the Mcm4/6/7 complex by negative staining. (A) The 600 kDa Mcm4/6/7 complex was purified from HeLa cells and subjected to native PAGE (i) and SDS-PAGE (ii) analyses to show the homogeneity of the complex. (B) A typical example of the electron micrograph obtained by negative staining, where the images denoted by arrows or by arrowheads were selected to obtain the averaged top-view or side view shown below. Bar = 100 nm. (C) Averaged images showing a toroid (i) or a slit (ii) of the human Mcm4/6/7 hexamer were obtained by the reference-free alignment method employing (i) 282 or (ii) 358 raw images, respectively. One of the six bulges found in (i) is split into two (denoted by an arrow). In (ii), a small bulge is observed between the two symmetrically related large bulges (denoted by an arrow). (D) An averaged toroidal image of the mouse Mcm4/6/7 hexamer obtained from 99 raw images. As in C-i, one of the bulges is split into two (denoted by an arrow). Bar = 5 nm for (C) and (D).

Two hybrid assay

Although previous reports have suggested that Mcm2 may form a homodimer by self-association in *Xenopus* and *S. pombe* (Prokhorova & Blow 2000; Sherman *et al.* 1998), in our experiments we found that human Mcm2 does not form a dimer by self-association (Fig. 3B, top panel). Instead, we found that Mcm6 interacts with itself (Fig. 3B, middle panel). To confirm these results, we performed yeast two-hybrid assays.

The open reading frames of the *MCM2*, *MCM4*, *MCM6* or *MCM7* genes were fused to the Gal4 activation

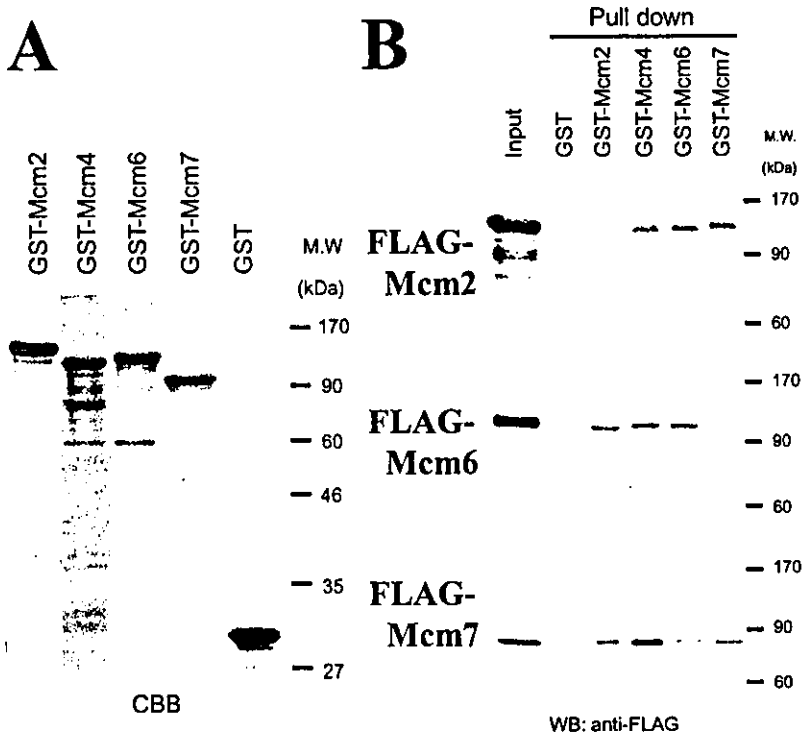

Figure 3 *In vitro* interactions between the Mcm2/4/6/7 subcomplexes. (A) Purified GST-fused Mcm2, 4, 6, 7 and GST alone bound to glutathione-Sepharose beads were separated on 10% SDS-PAGE, and proteins were stained with Coomassie Brilliant Blue. (B) Bacterial lysates expressing FLAG-tagged Mcm2, 6 and 7 proteins were incubated with GST-fused proteins on Sepharose beads as shown in (A). After precipitation and extensive washing of the beads, the bound fractions were analysed by Western blotting (WB) with anti-FLAG M2 antibody.

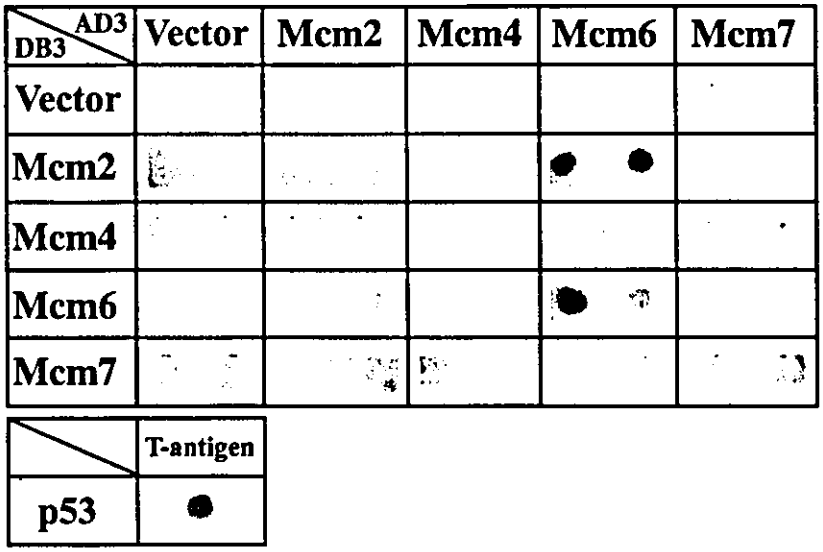

Figure 4 Two-hybrid analysis of the interactions between human Mcm proteins. Each Mcm protein fused to a DNA-binding domain (pDB3-Mcm2, 4, 6 or 7) was co-expressed in yeast strain Y190 with each Mcm protein fused to a Gal4-activating domain (pAD3-Mcm2, 4, 6 or 7) or vector alone (pAD3). The plasmid pair carrying p53 (pVA3) and T-antigen (pTD1) was used as a positive control. The β-galactosidase activity of the transformants carrying each plasmid pair was then assessed.

domain of pAD3 or the DNA binding domain of Gal4 domain in pDB3 (Tanaka *et al.* 2000). The relevant plasmid pairs were introduced into *S. cerevisiae* Y190 cells and the activity of the *LacZ* reporter gene was assessed. As shown in Fig. 4, when pAD3-Mcm6 and pDB3-Mcm6 were co-transformed, the resulting colonies turned blue in the presence of X-gal and IPTG, indicating that Mcm6 interacts directly with itself. A similar result was also obtained when pAD3-Mcm6 and pDB3-Mcm2 were combined. These results indicate that Mcm6 directly interacts with itself and Mcm2 in yeast cells. On the other hand, no apparent interaction was observed in other combinations, although it turned blue when the positive control plasmids (p53 and T-antigen) were

combined.This may be due to the weaker interactions in other combinations as compared to the Mcm6–Mcm6 or Mcm2–Mcm6 interaction.

Discussion

Mcm4/6/7 and Mcm2/4/6/7 complexes form toroidal structures

A number of DNA helicases isolated from both prokaryotes and eukaryotes function as hexamers, and electron microscopy shows that they form ring structures (Hingorani & O'Donnell 2000; Patel & Picha 2000). It has been suggested that the Mcm4/6/7 hexamer constitutes the replicative helicase, whereas the Mcm2, 3, 5 proteins have a regulatory function (Ishimi 1997; Schwacha & Bell 2001). We previously reported a rough image of an electron micrograph showing that the Mcm4/6/7 hexamer forms a toroidal structure with a central channel (Sato *et al.* 2000). In the present study, we present averaged fine images of electron micrographs showing that the Mcm4/6/7 hexamer has a symmetrical toroidal structure (Fig. 2C,D). The toroid is 13–14 nm in diameter and contains a central channel that is 3–4 nm in diameter.

In contrast to the eukaryotes, the archaeon (*Methanobacterium thermoautotrophicum*) genome contains only a single gene encoding Mcm protein (MtMcm) (Kelman *et al.* 1999). When this protein is purified, it assembles into large macromolecular complexes whose sizes suggest that they are double hexamers (Shechter *et al.* 2000). MtMCM was found to contain a helicase activity that preferentially uses dATP and DNA-dependent dATPase and ATPase activities (Shechter *et al.* 2000; Chong *et al.* 2000). The purified MtMCM protein formed a complex that shows a double hexamer under scanning transmission electron microscopy (Chong *et al.* 2000). It was shown that MtMCM can also assemble into a heptameric ring, containing a C-terminal helicase domain and an N-terminal domain of unknown function (Yu *et al.* 2002).

In addition, a more symmetrical structure (Fig. 2C-ii) was observed in the electron microscope analysis of the Mcm4/6/7 hexamer that might correspond to a side view of the hexamer. However, we cannot exclude the possibility that this symmetrical structure may also correspond to the top view, which would be indicative of a large conformational change in this complex. Such large transitions in subunit conformation have been reported for *E. coli* DnaB helicase (Yu *et al.* 1996). We also show here that the Mcm2/4/6/7 tetramer forms a similar but still distinct toroidal structure about 15–18 nm in diameter that has a central cavity of about 3–4 nm. It becomes asymmetrical when the Mcm2 protein, which is larger than the other three proteins, is joined as a partner (Fig. 1C-i, D-i).

Interactions between Mcm proteins in the toroidal structures

Using co-immunoprecipitation, *S. pombe* Mcm4 was shown to strongly interact with Mcm6 and weakly with Mcm2 (Sherman *et al.* 1998). Protein-protein cross-linking showed that fly Mcm2 interacts directly with Mcm5 and Mcm6; Mcm5 with Mcm3 and Mcm2; and Mcm6 with Mcm2 and Mcm4 (Crevel *et al.* 2001). Ishimi *et al.* (2001) showed that mouse Mcm2 interacts with mouse Mcm4 using Mcm proteins expressed in the rabbit reticulocyte. We confirmed their interactions using FLAG tagged human Mcm2 proteins with GST tagged human Mcm4 proteins (Fig. 3B; top panel). Since

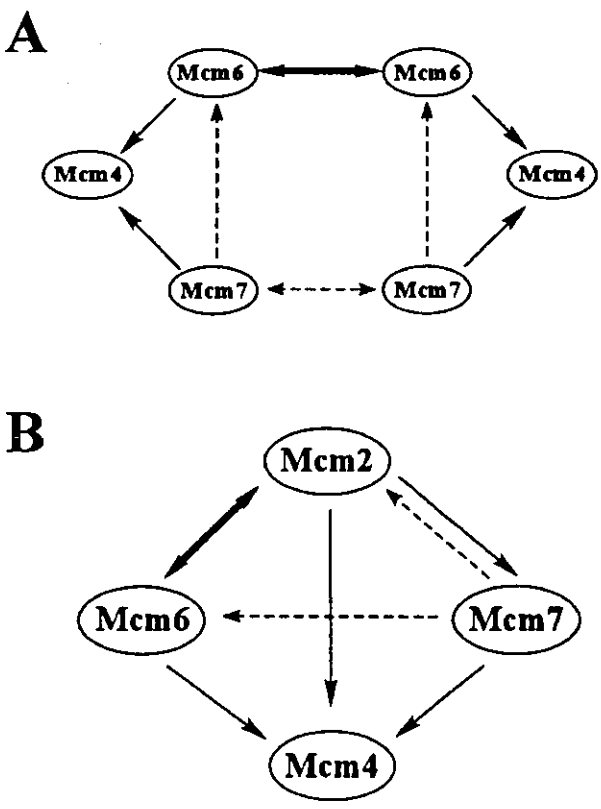

Figure 5 Proposed models of the order in which the proteins in the human Mcm4/6/7 (A) and Mcm2/4/6/7 (B) subcomplexes interact. Bold lines signify strong interactions that are detectable by both pull-down and two-hybrid assays; thin links for moderate interactions that are clearly detectable by pull-down assay; and dashed lines for weak interactions. Binary arrows indicate reciprocal associations.

these proteins were expressed in *E. coli* cells lacking Mcm proteins, we were able to demonstrate the direct interactions. We also confirmed the interactions of Mcm6 with Mcm2 and Mcm4 by GST-pull down experiments (Fig. 3B). Moreover, we found a self-interaction of Mcm6, not only in GST-pull down experiments, but also in two-hybrid analysis (Fig. 4). The results suggest that the Mcm proteins are arranged in the hexamer in the order Mcm7-Mcm4-Mcm6-Mcm6-Mcm4-Mcm7, with the putative Mcm6-Mcm6 hinge playing a significant role in the formation of this heterohexameric toroid.

The fractionation of extracts suggested that frog Mcm2 may form a homodimer by self-association (Prokhorova & Blow 2000). Although a truncated derivative of Mcm2 of *S. pombe* was able to self-associate in a two-hybrid assay, no evidence of this interaction has been reported *in vivo* (Sherman *et al.* 1998). Although we examined the interaction using affinity purified human Mcm2 protein, we could not detect its self-association (Fig. 3B, top panel). A two-hybrid analysis also failed to detect its self-interaction (Fig. 4). Thus, we conclude that, at least in humans, Mcm2 does not associate with itself.

Although both DNA helicase activity and DNA-dependent ATPase activity co-purify with the Mcm4/6/7 hexamer (Ishimi 1997), the heterohexameric Mcm complex that contains all six Mcm proteins from *S. pombe* harbours neither ATPase activity nor DNA helicase activity (Adachi *et al.* 1997). To explain this, it has been suggested that Mcm2 inhibits the DNA helicase activity of the Mcm4/6/7 hexamer by causing it to disassemble into Mcm2/4/6/7 tetramers (Ishimi *et al.* 1998). Supporting this, Sherman *et al.* (1998) reported that the Mcm2 of *S. pombe* associates with the Mcm4/6/7 complex via multiple domains *in vivo*. It was also indicated that the DNA helicase activity is intrinsically associated with the Mcm4/6/7 hexameric complex (You *et al.* 1999). The mutational analysis discriminates between two functionally distinct MCM protein subcomplexes, where the Mcm4/6/7 complex contributes canonical ATP binding motifs essential for catalysis, whereas the related motifs in Mcm2, 3 and 5 proteins serve a regulatory function (Schwacha & Bell 2001). You *et al.* (2002) reported that Mcm7 contributes to the DNA helicase activity of the Mcm complex by interacting with other subunits, whereas the zinc-finger of Mcm4 is involved in the subunit interactions of Mcm4/6/7 trimers. These observations all suggest that each Mcm protein in the complex plays distinct roles, and that Mcm2 inhibits the DNA helicase activity of the Mcm4/6/7 hexamer by inducing it to undergo a conformational transition into Mcm2/4/6/7 tetramers. Our study also supports this proposal.

Taken together, our results suggest that the Mcm proteins in the Mcm4/6/7 toroid must bind in the order Mcm7-Mcm4-Mcm6, since Mcm7 binds more strongly to Mcm4 than to Mcm6 (Fig. 5A). Furthermore, our data suggest that the self-association of Mcm6 may contribute to the formation of the Mcm7/4/6/6/4/7 heterohexamer. The interaction of Mcm6 and Mcm2 demonstrated here suggests that the Mcm proteins in the Mcm2/4/6/7 toroid are associated in the order Mcm2-Mcm6-Mcm4-Mcm7 (Fig. 5B). We tentatively propose that Mcm2 interactes with Mcm6 and can thereby disrupt the Mcm6-Mcm6 hinge. This may then cause the weak Mcm7-Mcm7 bond to break up, thus yielding the Mcm2/6/4/7 complex.

Experimental procedures

Plasmid constructs

To obtain cDNAs of the human *MCM2*, *MCM4*, *MCM6* and *MCM7* genes that carry in-frame *Asc*I-*Not*I sites, a set of oligonucleotides consisting of sequences around the initiation codon (plus *Asc*I site) and the stop codon (plus *Not*I site) of each *MCM* were synthesized and used as PCR primers (Tsuruga *et al.* 1997a,b). All the amplified sequences were checked for sequence fidelity by DNA sequencing. These cDNA inserts were introduced into the *Asc*I-*Not*I sites of the pGST6P, pMAC3B, pDB3 and pAD3 vectors. pGST6P was derived from pGEX6P (Amersham Pharmacia Biotech, Uppsala, Sweden) by the insertion of an *Asc*I site in the *Bam*HI site. pMAC3B was derived from pFLAG-MAC (Sigma, St Louis, MO, USA) by inserting an extra multiple cloning site between the *Tth*111I and *Xho*I sites. For the yeast two-hybrid assays, pDB3 and pAD3 were derived from pGBT9 and pGAD424 (Clontech, Palo Alto, CA, USA), respectively, by inserting an extra multiple cloning site between the *Eco*RI and *Sal*I sites.

Expression and purification of recombinant proteins

To express the FLAG-tagged Mcm2, Mcm6 and Mcm7 proteins, pMAC3B plasmids with the relevant Mcm cDNAs were introduced into bacteria (PR745 or BL21RIL). The cultures were induced with 0.1 mM isopropyl β-D-thiogalactopyranoside (IPTG) and incubated at 20 °C for 22 h. Cells were collected and resuspended in Extraction buffer A (50 mM Tris-HCl [pH 8.0], 5 mM EDTA, 0.25 mg/mL lysozyme, 1 mM PMSF) and then incubated at room temperature for 10 min. After adding a 1/10 volume of Extraction buffer B (1.5 M NaCl, 100 mM $CaCl_2$, 100 mM $MgCl_2$, 4 U DNase I, 1 μg/mL pepstatin A), the lysate was incubated at room temperature for 5 min and then centrifuged at 15 000 *g* for 1 h. To express glutathione-*S*-transferase (GST)-fused Mcm proteins, pGST6P plasmids with the appropriate cDNAs were introduced into bacteria. The cultures were induced with 0.1 mM IPTG and incubated at 20 °C for 20 h. Cells were collected and lysed in PBS containing 1% Triton X-100, 2 μg/mL leupeptin, 10 μg/mL aprotinin, 1 mM PMSF, 1 mM benzamidine, 1 mM NaF

Fujita, M., Kiyono, T., Hayashi, Y. & Ishibashi, M. (1997) *In vivo* interaction of human MCM heterohexameric complexes with chromatin. Possible involvement of ATP. *J. Biol. Chem.* **272**, 10928–10935.

van Heel, M., Harauz, G., Orlova, E.V., Schmidt, R. & Schatz, M. (1996) A new generation of the IMAGIC image processing system. *J. Struct. Biol.* **116**, 17–24.

Hingorani, M.M. & O'Donnell, M. (2000) A tale of toroids in DNA metabolism. *Nature Rev. Mol. Cell Biol.* **1**, 22–30.

Ishimi, Y. (1997) A DNA helicase activity is associated with an MCM4-6, and -7 protein complex. *J. Biol. Chem.* **272**, 24508–24513.

Ishimi, Y., Komamura, Y., You, Z. & Kimura, H. (1998) Biochemical function of mouse minichromosome maintenance 2 protein. *J. Biol. Chem.* **273**, 8369–8375.

Ishimi, Y., Komamura-Kohno, Y., Arai, K.-I. & Masai, H. (2001) Biochemical activities associated with mouse Mcm2 protein. *J. Biol. Chem.* **276**, 42744–42752.

Ishimi, Y., Komamura-Kohno, Y., You, Z., Omori, A. & Kitagawa, M. (2000) Inhibition of Mcm4,6,7 helicase activity by phosphorylation with cyclin A/Cdk2. *J. Biol. Chem.* **275**, 16235–16241.

Kelman, Z., Lee, J.K. & Hurwitz, J. (1999) The single minichromosome maintenance protein of *Methanobacterium thermoautotrophicum* DeltaH contains DNA helicase activity. *Proc. Natl. Acad. Sci. USA* **96**, 14783–14788.

Lee, D.G. & Bell, S.P. (2000) ATPase switches controlling DNA replication initiation. *Curr. Opin. Cell Biol.* **12**, 280–285.

Lee, J.K. & Hurwitz, J. (2000) Isolation and characterization of various complexes of the minichromosome maintenance proteins of *Schizosaccharomyces pombe*. *J. Biol. Chem.* **275**, 18871–18878.

Lei, M. & Tye, B.K. (2001) Initiating DNA synthesis: from recruiting to activating the MCM complex. *J. Cell Sci.* **114**, 1447–1454.

Ludtke, S.J., Baldwin, P.R. & Chiu, W. (1999) EMAN: semi automated software for high-resolution single-particle reconstructions. *J. Struct. Biol.* **128**, 82–97.

Nishitani, H. & Lygerou, Z. (2002) Control of DNA replication licensing in a cell cycle. *Genes Cells* **7**, 523–534.

Ogura, T. & Wilkinson, A.J. (2001) AAA+ superfamily ATPases: common structure—diverse function. *Genes Cells* **6**, 575–597.

Patel, S.S. & Picha, K.M. (2000) Structure and function of hexameric helicases. *Annu. Rev. Biochem.* **69**, 651–697.

Penczek, P., Radermacher, M. & Frank, J. (1992) Three-dimensional reconstruction of single particles embedded in ice. *Ultramicroscopy* **40**, 33–53.

Prokhorova, T.A. & Blow, J.J. (2000) Sequential MCM/P1 subcomplex assembly is required to form a heterohexamer with replication licensing activity. *J. Biol. Chem.* **275**, 2491–2498.

Sato, M., Gotow, T., You, Z., *et al.* (2000) Electron microscopic observation and single-stranded DNA binding activity of the Mcm4,6,7 complex. *J. Mol. Biol.* **300**, 421–431.

Sawaya, M.R., Guo, S., Tabor, S., Richardson, C.C. & Ellenberger, T. (1999) Crystal structure of the helicase domain from the replicative helicase-primase of bacteriophage T7. *Cell* **99**, 167–177.

Schwacha, A. & Bell, S.P. (2001) Interactions between two catalytically distinct MCM subgroups are essential for coordinated ATP hydrolysis and DNA replication. *Mol. Cell* **8**, 1093–1104.

Shechter, D.F., Ying, C.Y. & Gautier, J. (2000) The intrinsic DNA helicase activity of *Methanobacterium thermoautotrophicum* delta H minichromosome maintenance protein. *J. Biol. Chem.* **275**, 15049–15059.

Sherman, D.A., Pasion, S.G. & Forsburg, S.L. (1998) Multiple domains of fission yeast Cdc19p (MCM2) are required for its association with the core MCM complex. *Mol. Biol. Cell* **9**, 1833–1845.

Tanaka, Y., Okuzaki, D., Yabuta, N., Yoneki, T. & Nojima, H. (2000) Rad24 is essential for proliferation of diploid cells in fission yeast. *FEBS Lett.* **472**, 254–258.

Tsuruga, H., Yabuta, N., Hashizume, K., Ikeda, M., Endo, Y. & Nojima, H. (1997b) Expression, nuclear localization and interaction of human MCM/P1 proteins and the chromosomal mapping of their genes. *Biochim. Biophys. Res. Commun.* **236**, 118–125.

Tsuruga, H., Yabuta, N., Hosoya, S., Tamura, K. & Nojima, H. (1997a) HsMCM6: a new member of the human MCM/P1 family encodes a protein homologous to fission yeast Mis5. *Genes Cells* **2**, 381–399.

You, Z., Ishimi, Y., Masai, H. & Hanaoka, F. (2002) Roles of Mcm7 and Mcm4 subunits in DNA helicase activity of mouse Mcm4/6/7 complex. *J. Biol. Chem.* **277**, 42471–42479.

You, Z., Komamura, Y. & Ishimi, Y. (1999) Biochemical analysis of the intrinsic Mcm4-Mcm6-Mcm7 DNA helicase activity. *Mol. Cell. Biol.* **12**, 8003–8015.

Yu, X., Jezewska, M.J., Bujalowski, W. & Egelman, E.H. (1996) The hexameric *E. coli* DnaB helicase can exist in different Quaternary states. *J. Mol. Biol.* **259**, 7–14.

Yu, X., VanLoock, M.S., Poplawski, A., *et al.* (2002) The *Methanobacterium thermoautotrophicum* MCM protein can form heptameric rings. *EMBO Rep.* **3**, 792–797.

Received: 24 December 2002
Accepted: 29 January 2003

and 1 mM Na_3VO_4 by brief sonication. After centrifugation, the clear lysate was absorbed to Glutathione Sepharose 4B (Amersham Pharmacia Biotech). The proteins bound to the Sepharose beads were used for the pull-down assay.

Purification of Mcm proteins

For electron microscopy of human Mcm proteins, we purified the Mcm proteins in 0.2 M NaCl-soluble whole cell extracts of HeLa cells (six little cultures) by a series of procedures, namely, precipitation with ammonium sulphate, DE52 column chromatography, bovine serum albumin–Sepharose chromatography, histone H3/H4-Sepharose column (8 mL column) chromatography, followed by glycerol gradient centrifugation as reported previously (Ishimi 1997). Briefly, the proteins were eluted from the H3/H4 column by a linear NaCl gradient ranging from 0.3 M to 2 M. The Mcm protein fractions (12 mL) eluted from the H3/H4 column by 0.6–1 M NaCl were pooled and concentrated 10-fold with six Centricon 30 columns (Amicon). The concentrated samples were then diluted fivefold with a glycerol gradient buffer lacking NaCl to reduce the concentration of NaCl to 0.15 M. The sample was again concentrated with Centricon 30 columns to a volume of 0.2 mL, which was then separated by glycerol gradient centrifugation (Ishimi 1997).

For the electron microscopy of mouse Mcm complexes (Fig. 1C), the Mcm2/4/6/7 and Mcm4/6/7 complexes were prepared from insect cells co-infected with two recombinant baculoviruses containing the mouse *MCM2, 4, 6* and 7 genes and *MCM4, 6* and 7 genes, respectively (You *et al.* 1999).

Electron microscopy

The Mcm solutions were diluted with buffer (20 mM Tris-HCl [pH 7.5], 150 mM NaCl, 1 mM dithiothreitol, 0.5 mM EDTA, and 0.01% Triton X-100) to 10 μg/mL, after which each sample was applied on to a grid and negatively stained with 2% (w/v) uranyl acetate. The specimens were examined using a JEOL JEM 100CX electron microscope equipped with a LaB_6 filament operating at 100 kV. The electron micrographs were recorded on FG films at a nominal magnification of ×48 000 using defocus values of 0.7–1.1 μm. The recorded images were examined by optical diffraction to select images without drift or astigmatism, which were then digitized at a step size of 7.2 μm (corresponding to 1.5 Å of the specimen) using a CCD camera (DSScanner 1010).

All the Mcm2/4/6/7 particle images were extracted from three electron micrographs using EMAN (Ludtke *et al.* 1999) and analysed on SGI Workstations (Octane and Octane2) using the EM image analysis software package IMAGIC (van Heel *et al.* 1996). To detect variations in the particle images, multivariate statistical analysis (MSA) and hierarchic ascendant classification (HAC) of the images were performed. The particles within each class were summed and the resulting class averages were used to align the entire data set translationally and rotationally. Four cycles of MSA, HAC and alignment led to stable classes. Mcm4/6/7 particles images were extracted manually and analysed using SPIDER and WEB (Frank *et al.* 1996). The average images were obtained by averaging images aligned with the reference free alignment method (Penczek *et al.* 1992).

Pull-down assay and Western blotting

For the pull-down assay, the GST-Mcm proteins bound to Sepharose beads were washed twice with ice-cold PBS and then equilibrated with Extraction buffer A+B (10 : 1). The Sepharose beads were incubated at 25 °C for 1 h with bacterial lysate (from 5 mL of culture) expressing FLAG-Mcm protein. After extensive washing with Extraction buffer A+B (10 : 1) containing 0.1% Nonidet P-40, the bound fractions were resolved by 10% SDS-PAGE and transferred to PVDF membranes (Millipore, Bedford, MA, USA). Western blotting was performed with 2 μg of anti-FLAG M2 antibody (Sigma) or anti-GST monoclonal antibody (MBL Co. Ltd, Ina, Nagano, Japan) in TBST (100 mM Tris-HCl [pH 7.5], 150 mM NaCl, 0.05% Tween-20) containing 5% skim milk.

Yeast two-hybrid assay

Yeast strain Y190 was transformed with pDB3-human *MCMs* and pAD3-human *MCMs* and the transformants were selected on plates lacking tryptophan, leucine and uracil as previously described (Tanaka *et al.* 2000). Colonies thus isolated were patched on to a medium lacking the same amino acids. After growth, the colonies were spotted on to a filter paper and then immersed in liquid nitrogen. These colonies were subjected to the β-galactosidase assay. Positive control plasmid DNAs that carried p53 (pVA3) and T-antigen (pTD1) were purchased (Clontech).

Acknowledgements

We thank Dr P. Hughes for a critical reading of the manuscript and Dr Z. You for preparation of the mouse Mcm2/4/6/7 complex. We thank Mr I. Nagamori and Ms K. Ikeue for experimental assistance. This work was supported by a Grant-in-Aid for Scientific Research on Priority Areas from the Ministry of Education, Culture, Sports, Science and Technology of Japan to H.N.

References

Adachi, Y., Usukura, J. & Yanagida, M. (1997) A globular complex formation by Nda1 and the other five members of the MCM protein family in fission yeast. *Genes Cells* **2**, 467–479.

Chong, J.P., Hayashi, M.K., Simon, M.N., Xu, R.M. & Stillman, B. (2000) A double-hexamer archaeal minichromosome maintenance protein is an ATP-dependent DNA helicase. *Proc. Natl. Acad. Sci. USA* **97**, 1530–1535.

Crevel, G., Ivetic, A., Ohno, K., Yamaguchi, M. & Cotterill, S. (2001) Nearest neighbor analysis of MCM protein complexes in *Drosophila melanogaster*. *Nucl. Acids Res.* **29**, 4834–4842.

Frank, J., Radermacher, M., Penczek, P., *et al.* (1996) SPIDER and WEB: processing and visualization of images in 3D electron microscopy and related fields. *J. Struct. Biol.* **116**, 190–199.

Fission yeast *meu14⁺* is required for proper nuclear division and accurate forespore membrane formation during meiosis II

Daisuke Okuzaki[1,*], Wataru Satake[1,*], Aiko Hirata[2] and Hiroshi Nojima[1,‡]

[1]Department of Molecular Genetics, Research Institute for Microbial Diseases, Osaka University, 3-1 Yamadaoka, Suita, Osaka 565-0871, Japan
[2]Department of Integrated Biosciences, Graduate School of Frontier Sciences Tokyo University, Bldg. FSB-101/601, 5-1-5 Kashiwanoha, Kashiwa, Chiba 277-8562, Japan

*These authors contributed equally to this work
‡Author for correspondence (e-mail: hnojima@biken.osaka-u.ac.jp)

Accepted 18 March 2003
Journal of Cell Science 116, 2721-2735 © 2003 The Company of Biologists Ltd
doi:10.1242/jcs.00496

Summary

Using a meiosis-specific subtracted cDNA library of *Schizosaccharomyces pombe*, we identified *meu14⁺* as a gene whose expression is upregulated during meiosis. Transcription of *meu14⁺* is induced abruptly after the cell enters meiosis. Its transcription is dependent on the meiosis-specific transcription factor Mei4. In *meu14Δ* cells, the segregation and modification of the SPBs (spindle pole bodies) and microtubule elongation during meiosis II were aberrant. Meiotic *meu14Δ* cells consequently produced a high frequency of abnormal tetranucleate cells harboring aberrant forespore membranes and failed to produce asci. In wild-type cells harboring the integrated *meu14⁺-gfp* fusion gene, Meu14-GFP first appeared inside the nuclear region at prophase II, after which it accumulated beside the two SPBs at metaphase II. Thereafter, it formed two ring-shaped structures that surrounded the nucleus at early anaphase II. At post-anaphase II, it disappeared. Meu14-GFP appears to localize at the border of the forespore membrane that later develops into spore walls at the end of sporulation. This was confirmed by coexpressing Spo3-HA, a component of the forespore membrane, with Meu14-GFP. Taken together, we conclude that *meu14⁺* is crucial in meiosis in that it participates in both the nuclear division during meiosis II and the accurate formation of the forespore membrane.

Movies available online

Key words: Meiosi, Spore formation, Forespore membrane, Microtubule, Spindle pole body, *Schizosaccharomyces pombe*

Introduction

Meiosis produces haploid gametes in eukaryotic organisms through two successive meiotic divisions. The fission yeast *Schizosaccharomyces pombe* is a useful model organism to study the mechanisms that regulate processes that occur during meiosis (e.g. recombination, chromosome behavior, and sporulation) because it synchronously enters meiosis and can be easily manipulated by a variety of genetical and cell biological techniques. Meiosis in fission yeast is initiated when haploid cells of opposite mating types (h^-/h^+) experience nitrogen starvation and conjugate (Moreno et al., 1991). Following karyogamy (nuclear fusion), premeiotic DNA synthesis occurs. The nucleus then develops a 'horse-tail' shape and moves backwards and forwards about the axis of the cell. This permits homologous pairing and recombination to take place (Chikashige et al., 1994). Successive nuclear divisions, called meiosis I and meiosis II, then ensue. After meiosis II, the capsular plasma membrane forms round each haploid nucleus in the cytoplasm of the mother cell, after which spore formation occurs to generate four mature ascospores.

Spore formation is initiated during meiosis II in that during this division, the dividing nuclei start to be surrounded by a double unit membrane, called the forespore membrane. A previous study has shown that the forespore membrane develops near the outer plaques of the spindle pole body (SPB) during meiosis II and plays an important role in the packaging of the haploid nucleus (Hirata and Shimoda, 1994) However, the exact molecular mechanism driving forespore membrane development is unclear.

For efficient spore production, the formation of the forespore membrane must be coordinated with the behavior of the dividing nuclei during meiosis II. The SPB is thought to be a key structure that links these two events. The SPB may act similarly to the mammalian centrosome, which functions as a microtubule-organizing center (MTOC). The SPB enters and leaves the nuclear envelope during the cell cycle (Ding et al., 1997), and has been observed by immunostaining to change from a dot-like image into a crescent during meiosis II (Hirata and Shimoda, 1994; Hagan and Yanagida, 1995). The correct morphological alteration of the SPB and the resulting normal sporulation depends on Spo15, an SPB component that is essential for forespore membrane formation (Ikemoto et al., 2000). Electron microscopic observation has revealed that the forespore membrane is initially assembled next to the SPB, which changes morphologically into a multilayered structure during meiotic division II (Tanaka and Hirata, 1982; Hirata and

Shimoda, 1994; Hagan and Yanagida, 1995). This suggests that SPB modification is required to initiate forespore membrane formation. Thus, SPBs play an additional role in sporulation that is distinct from their known roles as MTOC scaffolds in mitosis and meiotic division I.

Other molecules that appear to be required for normal sporulation are Spo20, an *S. pombe* phosphatidylinositol-transfer protein (Nakase et al., 2001), Spo3, a forespore membrane component (Nakamura et al., 2001), and Meu10, a molecule with no homology to well-characterized proteins (Tougan et al., 2001). Thus, sporulation appears to consist of several cytologically distinct steps that include the modification of SPBs, the assembly of forespore membranes around the SPBs, the enclosure of nuclei by the forespore membranes, the maturation of the spore wall, and the autolysis of the ascus wall. With regard to the forespore membrane, it is assembled by the fusion of vesicles perhaps derived from the endoplasmic reticulum (ER) and/or the Golgi apparatus (Tanaka and Hirata, 1982; Hirata and Shimoda, 1994). However, little is known about how the forespore membrane assembles in fission yeast, which is in contrast to the prolific studies examining the same phenomenon in budding yeast (for a review, see Pringle et al., 1997).

To understand how meiosis and sporulation are regulated in *S. pombe* in more detail, we have established a subtracted cDNA library to comprehensively isolate meiosis/sporulation-specific genes that we have denoted as meu (meiotic expression upregulated) (Watanabe et al., 2001). Previously, we reported that the gene product generated from one of these genes, meu13$^+$, promotes homologous pairing independently of homologous recombination and regulates the meiotic recombination checkpoint (Nabeshima et al., 2001; Shimada et al., 2002). Furthermore, we found that the meu10$^+$ product is required for ascospore maturation (Tougan et al., 2001). Here, we characterize another meu gene, meu14$^+$. We show that the *S. pombe* Meu14 protein is expressed specifically during sporulation and appears to play a role in the extension of the forespore membrane and perhaps also in the function of the SPB and/or the meiotic spindles.

Materials and Methods

Cells and media

The *S. pombe* strains used in this study are listed in Table 1. Cells were grown as described previously (Nabeshima et al., 2001). Malt extract medium (MEA) and synthetic medium (EMM2) with the appropriate auxotrophic nutrients were used for mating between the h^- and h^+ strains and maintenance of diploidy. To observe meiosis, h^-/h^+ diploid and h^{90} cells were cultured in EMM2 with the appropriate auxotrophic nutrients, washed in EMM-N medium (EMM2 without nitrogen) and then incubated at 28°C in EMM-N (Moreno et al., 1991).

Isolation and deletion of *meu14*$^+$

The genomic library (Fukushima et al., 2000) was made using partial *Sau*3AI DNA fragments inserted into the *Bam*HI site of the Bluescript KS(+) vector (Stratagene, La Jolla, CA). Colony hybridization with the *meu14*$^+$ cDNA fragment as a probe allowed us to clone the genomic fragment containing the *meu14*$^+$ gene from this library. To disrupt *meu14*$^+$, a 1.1 kb *Nsp*I fragment carrying the *meu14*$^+$ genomic DNA was replaced with the 1.8 kb *Hin*dIII fragment containing *ura4*$^+$ using a synthetic linker. The *meu14*$^+$*::ura4*$^+$ DNA fragment digested with *Kpn*I (−1104 bp site from start codon) and *Pst*I (1050 bp site from stop codon) was used to transform wild-type cells (TP4D-5A/TP4D-1D). This procedure removed all of the coding region of Meu14, including the initiation codon. The Ura$^+$ transformants were then screened for the disruption of one of the *meu14*$^+$ gene copies by genomic Southern blot analysis. Tetrads from these cells were then dissected. Northern and Southern blot analyses were performed as described previously (Watanabe et al., 2001).

Preparation of Meu14-GFP

The Meu14 protein fused C-terminally with the green fluorescence protein (GFP) was made by first synthesizing oligonucleotides FN (5′-GGCGCGCCGCATATGGGCACTCAACCATCTTAC-3′) and FC (5′-GCGGCCGCCGGCAAGAAAACAGTGGATTTTGC-3′), which correspond to the initiation and termination sites of Meu14, respectively. The *Nde*I and *Not*I sites introduced into the oligonucleotides are underlined, respectively. Using these oligonucleotides as primers and *meu14*$^+$ genomic DNA as a template, we performed a polymerase chain reaction (PCR) and generated a

Table 1. *S. pombe* diploid strains used in this study

Name	Genotype	Source
CD16-1	*h*$^+$*/h*$^-$ *ade6-M210/ade6-M216 cyh1/+ +/lys5-391*	Nabeshima et al., 2001
CD16-5	*h*$^-$*/h*$^-$ *ade6-M210/ade6-M216 cyh1/+ +/lys5-391*	Nabeshima et al., 2001
JZ670	*h*$^-$*/h*$^-$ *pat1-114/pat1-114 ade6-M210/ade6-M216 leu1-32/leu1-32*	Nabeshima et al., 2001
AB4	*h*$^-$*/h*$^-$ *pat1-114/pat1-114 ade6-M210/ade6-M216 leu1-32/leu1-32 ura4-D18/ura4-D18 mei4::ura4*$^+$*/mei4::ura4*$^+$	Abe and Shimoda, 2000
TN187	*h*^{90} *spo3-HA:LEU2 leu1-32 ura4-D18*	Nakamura et al., 2001
TP4D-5A/ TP4D-1D	*h*$^-$*/h*$^+$ *ade6-M210/ade6-M216 leu1-32/leu1-32 ura4-D18/ura4-D18 +/his2*	Watanabe et al., 2001
YDO100	*h*$^-$*/h*$^+$ *ade6-M210/ade6-M216 leu1-32/leu1-32 ura4-D18/ura4-D18 +/his2 meu14*$^+$*::ura4*$^+$*/ meu14*$^+$*::ura4*$^+$	This study
YDO110	*h*$^-$*/h*$^+$ *ade6-M210/ade6-M216 leu1-32/leu1-32 ura4-D18/ura4-D18 +/his2 spo15-GFP:LEU2/spo15-GFP:LEU2*	This study
YDO111	*h*$^-$*/h*$^+$ *ade6-M210/ade6-M216 leu1-32/leu1-32 ura4-D18/ura4-D18 +/his2 spo15-GFP:LEU2/spo15-GFP:LEU2 meu14::ura4*$^+$*/ meu14::ura4*$^+$	This study
YDO120	*h*$^-$*/h*$^+$ *ade6-M210/ade6-M216 leu1-32/leu1-32 ura4-D18/ura4-D18 +/his2 meu14*$^+$*:GFP/meu14*$^+$*:GFP*	This study
YDO121	*h*$^-$*/h*$^+$ *ade6-M210/ade6-M216 leu1-32/leu1-32 ura4-D18/ura4-D18 +/his2 meu14*$^+$*:GFP/meu14*$^+$*:GFP spo3-HA:LEU2/spo3-HA:LEU2*	This study
MKD3	*h*^{90} *spo3::ura4*$^+$ *leu1-32 ura4-D18*	Nakamura et al., 2001
YDO50	*h*^{90} *leu1-32 ura4-D18 meu14*$^+$*:GFP*	This study
YDO130	*h*^{90} *spo3::ura4*$^+$ *leu1-32 ura4-D18 meu14*$^+$*:GFP*	This study
S151	*h*^{90} *spo15::ura4*$^+$ *leu1-32 ura4-D18*	Ikemoto et al., 2000
YDO10	*h*^{90} *spo15*$^+$*::ura4*$^+$ *leu1-32 ura4-D18 meu14*$^+$*:GFP*	This study
YN68	*h*^{90} *leu1-32:GFP-psy1*$^+$	C. Shimoda (Osaka City University, Japan)
YDO150	*h*^{90} *leu1-32:GFP-psy1*$^+$ *ura4-D18 meu14::ura4*$^+$	This study

meu14$^+$ fragment harboring the *Nde*I and *Not*I sites in the N- and C-termini, respectively. After performing a TA-cloning procedure, this DNA fragment was digested by *Nde*I and *Not*I and inserted into the pRGT1 vector (a gift from M. Yamamoto, University of Tokyo), which was designed to fuse GFP to the insert if the DNA was inserted in-frame via *Nde*I/*Not*I sites using the pREP1 vector (Maundrell, 1993). For Meu14-GFP protein expression during vegetative growth, the *meu14*$^+$ DNA fragment generated by PCR to contain *Nde*I and *Not*I sites at the ends was inserted into pRGT81, a modified pRGT1 vector designed to carry a weak *nmt* promoter. This construct is termed pRGT81-*meu14*$^+$. To obtain the 5′ upstream promoter region of *meu14*$^+$, we performed PCR using the primers 5N (5′-CTGCAGA-TCCGAGCAAGAAGAGGCT-3′) and 5C (5′-CATATGGATTGTT-TACG TTTCAGA-3′). The *Pst*I and *Nde*I sites introduced into the oligonucleotides are underlined, respectively. The *nmt1* promoter between the *Pst*I and *Nde*I sites in the pRGT1-*meu14*$^+$ construct was replaced by this amplified DNA fragment. We picked four independent clones and determined the DNA sequences of the amplified regions in order to select the clone whose sequence does not contain point mutations introduced by the PCR amplification. This construct is termed pNP-*meu14*$^+$. Next, the *Nsp*I genomic DNA fragment corresponding to the 3′ downstream region of *meu14*$^+$ (+61 to 1138 bp from stop codon) was inserted into the *Sma*I site between the GFP gene and the *nmt1* terminator in the pNP-*meu14*$^+$ construct. This *meu14*$^+$-*gfp* DNA fragment carrying about 1 kb of both upstream and downstream regions was digested with *Pst*I and *Kpn*I, and then used to transform *meu14*$^+$::*ura4*$^+$ cells (YDO100). The Ura$^-$ transformants were obtained by screening for the clone that survived in the medium containing 5-Fruoroorotic Acid (5-FOA), which was confirmed by Southern blot analysis (data not shown).

Immunofluorescence

Meiotic cells were fixed following the procedure of Hagan and Hyams using glutaraldehyde and paraformaldehyde (Hagan and Hyams, 1988). In indirect immunofluorescence microscopy (Hagan and Yanagida, 1995), the SPB was stained with the anti-Sad1 antibody (a gift from M. Yanagida, University of Kyoto), microtubules were stained with the TAT-1 antibody [a gift from K. Gull, University of Manchester (Woods et al., 1989)], and the nuclear pore complex was stained with the MAb414 antibody (CRP, Denver, PA). Spo3-HA (a gift from C. Shimoda, City University of Osaka) was stained with the anti-HA antibody 3F10 (Boehringer Mannheim, Mannheim, Germany). Subsequently, a Texas-Red-conjugated sheep anti-mouse antibody (Amersham Biosciences, Piscataway, NJ) was used to visualize the microtubules, Spo3-HA, and the nuclear pore complex. An Alexa-488 or 594-conjugated goat anti-rabbit antibody (Molecular Probes, Eugene, OR), a Cy5-conjugated donkey anti-rabbit antibody (Jackson ImmunoResearch Laboratories, West Grove, PA), and a Texas-Red-conjugated donkey anti-rabbit antibody (Amersham Biosciences, Piscataway, NJ) were used to stain Sad1. The samples were then stained with 0.2 mg/ml DAPI or Hoechst 33342 in PBS for 5 minutes and mounted with antifade-containing Vectashield mounting medium (Vector Laboratories, Burlingame, CA). Fluorescence images of these cells were observed using a fluorescence microscope (Axiophot, Zeiss, Germany or BX51, Olympus, Tokyo, Japan) with a charge-coupled device (CCD) cameras (Photometrics PXL1400) or Cool SNAP CCD camera (Roper Scientific, Sad Diego, CA). Immunofluorescence images were acquired using Adobe PhotoShop 6.0.

Fluorescence in vivo imaging of Meu14 and chromosomes

To stain chromosomes and detect Meu14-GFP in living meiotic cells, *meu14*$^+$-*gfp* cells (YDO120) were first transferred to EMM2-N to induce meiosis. The meiotic cells were then stained with Hoechst 33342 (1.0 μg/ml) for a few minutes. Stained live cells were mounted on a coverslip by spotting, and microscopic observations were carried out with the Delta Vision microscope system (Applied Precision, Issaquah, WA). Images were taken with a 0.2 second exposure at 2 minute intervals. This system allows multi-color and three-dimensional acquisition of digitized images with a cooled CCD camera. The images of the live meiotic cells stained with Hoechst 33342 were obtained as described (Chikashige et al., 1994).

Preparation of cell extracts and immunoblotting

S. pombe cells (3.3×10^8 cells) were suspended in 0.3 ml of HB buffer (25 mM MOPS, pH 7.2, 15 mM $MgCl_2$, 15 mM EGTA, 60 mM β-glycerophosphate, 15 mM p-nitrophe-nylphosphate, 0.1 mM Na_3VO_4, 1 mM dithiothreitol, 1 mM phenylmethylsulf o-nylfluoride, and 20 mg each of leupeptin and aprotinin per ml) and disrupted with acid-washed glass beads using a bead beater. Proteins in the extracts were separated by SDS-PAGE and transferred onto polyvinylidene difluoride membranes (Immobilon; Millipore, Bedford, MA). Blots were probed with the rat anti-GFP antibody (a gift from S. Fujita of Mitsubishi Kagaku Institute of Life Sciences, Tokyo, Japan) and the rabbit anti-Cdc2 antibody (Santa Cruz Biotechnology, Santa Cruz, CA). The bands bound by the horseradish peroxidase-conjugated goat anti-rat IgG (Santa Cruz Biotechnology, Santa Cruz, CA) for the anti-GFP antibody or goat anti-mouse IgG (ICN Pharmaceuticals, Costa Mesa, CA) for the anti-Cdc2 antibody were visualized using the Renaissance system (NEN Life Sciences, Boston, MA).

Electron microscopic observations

Wild-type diploid (TP4D-5A/TP4D-1D) and *meu14Δ* diploid (YDO110) cells were grown in EMM2 medium at 33°C, transferred to EMM-N medium at 30°C, and harvested by centrifugation 6 or 8 hours later. The pelleted cells were cryofixed by high-pressure-freezing using a HPM 010 (Bal-Tec, Balzers, Liechtenstein) as previously described (Humbel et al., 2001) before being subjected to electron microscopy (Hitachi H-7600, Hitachi High-Technologies, Tokyo, Japan).

Results

The meu14$^+$ gene is expressed predominantly during meiosis

We identified meu14$^+$ as one of several *S. pombe* genes whose transcription is only upregulated in meiosis induced by nitrogen starvation using a meiosis-specific subtracted cDNA library (Watanabe et al., 2001). To test this, we took advantage of the fact that, upon nitrogen starvation, the heterozygous CD16-1 (h^+/h^-) strain initiates meiosis, while the homozygous CD16-5 (h^-/h^-) strain does not. Northern blot analysis using RNA from the CD16-1 and CD16-5 strains and a radiolabeled meu14$^+$ probe indeed showed that the meu14$^+$ transcript of 1.3 kb is detected only in the CD16-1 strain and that it emerges approximately 6-12 hours after nitrogen starvation (Fig. 1A). In this experiment, the progression through the various meiotic steps was monitored by counting the frequency of 4 nuclei at 2 hours intervals by fluorescence microscopy (Fig. 1A, bottom panel). Notably, no meu14$^+$ transcription was observed during the mitotic cell cycle (Fig. 1A,B, 0 hour time point). When we used pat1-114 cells, which synchronously initiate meiosis at the restrictive temperature, we detected the hybridized bands only at 6, 8 and 10 hours. The peak was at 8 hours, at which time many of the cells were between the two meiotic nuclear divisions, meiosis I and meiosis II (Fig. 1B). Thus, we conclude that meu14$^+$ begins to be expressed at some point between the two meiotic nuclear divisions.

Furthermore, we investigated whether meu14$^+$ gene expression occurs under the control of the meiosis-specific transcription regulator Mei4 because the Mei4 target sequence termed FLEX (GTAAACAAACAGA) occurs in the 5′ upstream region of meu14$^+$ (Horie et al., 1998; Abe and Shimoda, 2000). Northern blot analysis showed that meu14$^+$ gene expression was not detectable in the mei4Δ strain (Fig. 1B, right panel). This suggests that meu14$^+$ expression is under the direct control of Mei4.

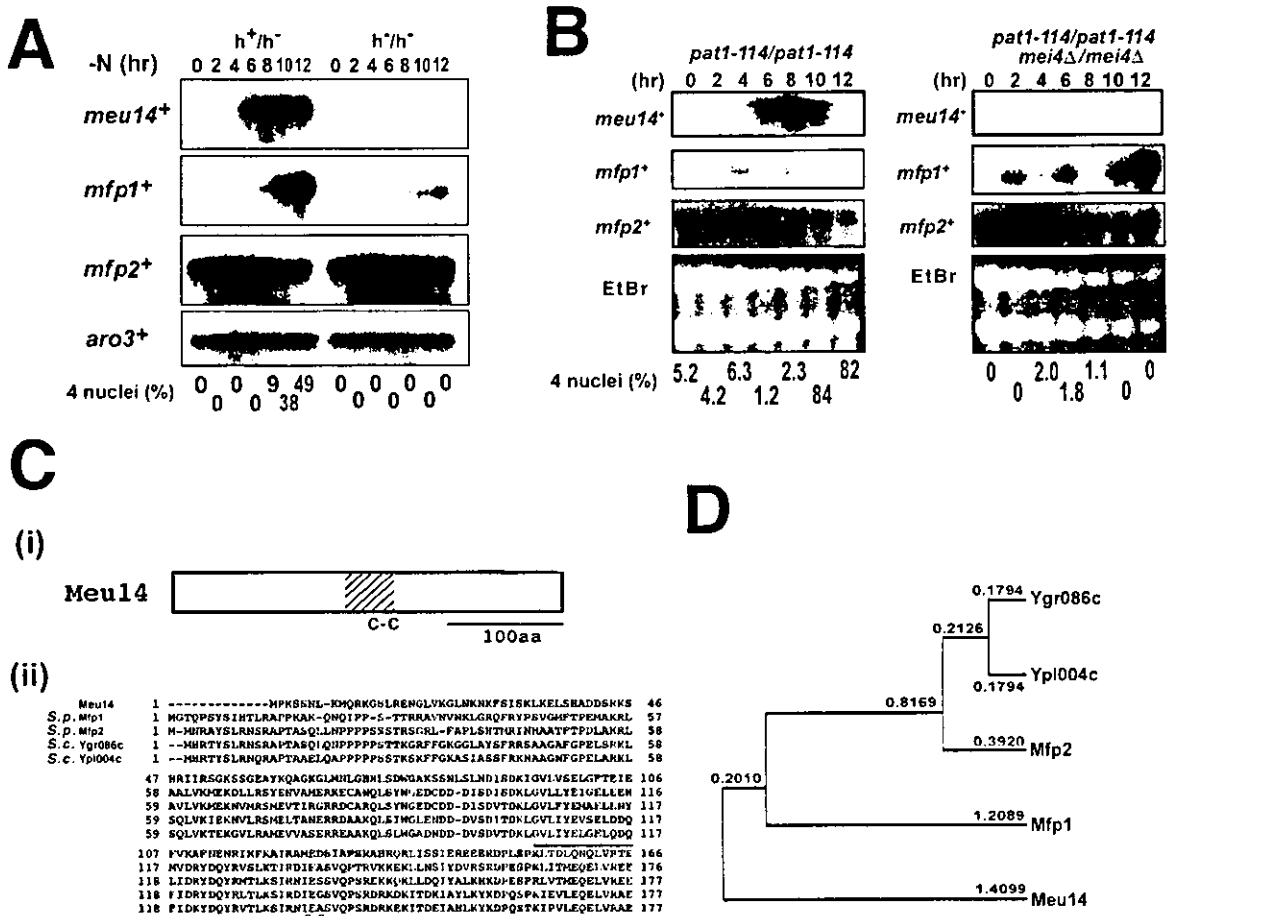

Fig. 1. Expression of *meu14*$^+$ and its paralogs during meiosis and structural comparison of their gene products. (A) The *meu14*$^+$ gene is specifically transcribed during meiosis. Diploid *h*$^+$/*h*$^-$ (CD16-1) and *h*$^-$/*h*$^-$ (CD16-5) cells were exposed to nitrogen starvation, which triggers meiosis in the former but not the latter strain, and cells were collected at 2 hour intervals for RNA extraction. Upper panels: Total RNA was blotted and probed by radiolabeled *meu14*$^+$, *mfp1*$^+$, *mfp2*$^+$ and *aro3*$^+$ DNA fragments. The intensities of the bands obtained by using the *aro3*$^+$ probe and ethidium bromide staining were used as loading controls. Numbers at the bottom represent the cell populations harvested at each 2 hour interval and assessed for the percentages of cells that had four nuclei (counted after staining the cells with DAPI). (B) *meu14*$^+$ gene expression is under the control of the sporulation-specific Mei4 transcription factor. Diploid *h*$^-$/*h*$^-$ *pat1-114/pat1-114* (JZ670) and *h*$^-$/*h*$^-$ *pat1-114 mei4Δ pat1-114 mei4Δ* (AB4) cells were synchronized to enter the G1 phase by nitrogen starvation, and then induced to meiosis by temperature shift. Nitrogen was then added, and the cells were incubated at 34°C and collected at 2 hour intervals for RNA analysis as in panel A. (C) Structure of Meu14. (i) Conserved structural motifs. The coiled-coil region (C-C) is predicted using the COILS program with a 21-residue window setting (Lupas et al., 1991). (ii) Alignment of the predicted amino acid sequence of Meu14 with *S. pombe* and *S. cerevisiae* homologues. Homologous proteins were identified in a BLAST search using the protein sequence of Meu14. Hyphens represent gaps inserted to attain maximal homology. Amino acids identical to those in Meu14 are highlighted by a gray background. Amino acid numbers are denoted at the right-hand side of each sequence. The extended coiled-coil motif found in Meu14 is indicated by a solid line. (D) The phylogenetic tree of the Meu14 homologues. The tree was constructed based on the whole amino acid sequence of each protein by Genetyx-Mac software (Software Development, Tokyo, Japan) using the neighbor joining method (Saitou and Nei, 1987). The genomic DNA sequences used are recorded in the DDBJ/EMBL/GenBank database (accession nos. CAA97088, AAB68101, CAB16733 and CAA19279, respectively).

Structural characterization of the meu14$^+$ gene and its product

We used the isolated *meu14$^+$* cDNA fragment as a probe to screen the genomic library of *h*$^-$ L972 cells (Fukushima et al., 2000). This allowed us to clone a DNA fragment that included the surrounding regions of the *meu14$^+$* gene, and the DNA sequence was determined (DDBJ accession No. AB016983). Comparison of the genomic DNA and cDNA sequences indicated that the *meu14$^+$* gene contains one intron-bearing consensus intron splice and branch sequences (data not shown). *meu14$^+$* encodes a predicted translation product consisting of 335 amino acids with a molecular weight of ~37 kDa. The PSORT II server program (http://psort.ims.u-tokyo.ac.jp/) was used to search for motifs and revealed that the Meu14 protein has a predicted coiled-coil (C-C) motif (Burkhard et al., 2001) in the central region of the molecule (Fig. 1Ci).

The BLAST algorism (http://www.genome.ad.jp/) was used to search for homologous genes and revealed that there are two genes in *S. pombe* that are paralogous to *meu14$^+$*. We have denoted them as *mfp1$^+$* (SPAC3C7.02C) and *mfp2$^+$* (SPCC736.15) after *meu* fourteen *p*aralog. Notably, an intimate homolog of *meu14$^+$* does not exist in the genome of *S. cerevisiae*. Maximum matching alignment (Fig. 1Cii) and a phylogenetic tree (Fig. 1D) based on the overall amino acid sequences of the proteins clearly show that the Mfp1 and Mfp2 proteins are more similar to the budding yeast homologues Ygr086c and Yp1004c than to Meu14. Genes with obvious homology to *meu14$^+$* have not been identified in any other organism.

Northern blot analysis indicated that, like *meu14$^+$*, *mfp1$^+$* transcription is only induced during the meiosis/sporulation process, although it was expressed later (8-12 hours; Fig. 1A). It is strange, however, that when the *pat1-114* strain is used, *mfp1$^+$* displays two peaks (Fig. 1B). We obtained this result repeatedly using different northern blots. The reason for this is currently under investigation. Nevertheless, when we constructed a null mutation of *mfp1$^+$*, abnormal phenotypes in vegetative growth or the meiosis/sporulation of diploid cells were not observed (data not shown). With regard to *mfp2$^+$*, northern blot analysis revealed that it is transcribed both during vegetative growth (0 hours) and meiosis (Fig. 1A). Moreover, neither *mfp1$^+$* nor *mfp2$^+$* seems to be under the control of Mie4 transcription factor (Fig. 1B, right panel). Thus, *mfp1$^+$* and *mfp2$^+$* genes were not studied further.

meu14Δ cells fail to sporulate and produce a high frequency of abnormal tetranucleated cells

To assess the physiological role of meu14$^+$, a deletion mutant that expresses no Meu14 protein was constructed by one-step gene replacement (see Materials and Methods). We confirmed the successful disruption of meu14$^+$ by examining the transformants for the presence or absence of the uracil auxotrophic marker and by Southern analysis.

Diploid cells in which one of the *meu14$^+$* genes had been replaced by *ura4$^+$* were sporulated and germinated. The segregation ratio compared to the wild-type was 1:1. All of the resulting spores were viable, indicating that the *meu14$^+$* gene is not essential for vegetative growth. The growth properties and the cell size and morphology of *meu14Δ* cells were also indistinguishable from those of the wild-type cells. Thus, we conclude that the *meu14$^+$* gene has no obvious function in the vegetative growth phase.

FACS analysis indicated that premeiotic DNA synthesis was normal in meu14Δ cells (data not shown). Spore walls were not formed by diploid cells homozygous for the meu14Δ gene (Fig. 2A,B), indicating that meu14Δ cells are defective in sporulation. Progression through the various meiotic steps was monitored by counting the frequency of various numbers of nuclei at 2 hour intervals by fluorescence microscopy and showed that meu14Δ cells proceed normally through the onset of the two meiotic divisions, as its kinetics are comparable to that of the parental wild-type control (Fig. 2C). Thus, the onset of the nuclear divisions occurring during meiosis I and II is normal in meu14Δ cells. However, at 12 hours, at which point 80% of the wild-type cells had undergone sporulation, no asci were observed in meu14Δ cells, confirming sporulation in meu14Δ cells is severely impaired. Notably, horse-tail phase seems longer in meu14Δ cells than wild-type, which suggests that Meu14 may also play a role at this phase. The meu14Δ cells produced abnormal tetranucleate cells at a high frequency (Fig. 2D). We could classify these abnormal tetranucleate cells into five classes (see legend to Fig. 2D). Taken together, we conclude that meu14Δ cells become abnormal after meiosis II has commenced.

SPB assembly is aberrant in meu14Δ cells during meiosis II

To determine if the abnormal tetranucleate cells of *meu14Δ* strain are due to the aberrant function of the microtubules or the SPBs, *meu14Δ* cells were induced to enter meiosis. The cell populations enriched in anaphase II cells were then stained by Hoechst 33342 to reveal the nuclei and immunostained with the anti--tubulin antibody (TAT-1) and the anti-Sad1 antibody to delineate the microtubules and the SPBs (Hagan and Yanagida, 1995), respectively. We found that *meu14Δ* cells are normal at meiosis I (Fig. 3Av,vi). However, many of the *meu14Δ* cells progressing though meiosis II contained fragmented or unequally-shaped microtubule bundles (Fig. 3Ai-iv). Moreover, multiple Sad1-stained objects were observed more frequently in *meu14Δ* cells (Fig. 3A)

To confirm that the anti-Sad1 antibody specifically recognize the SPBs in meu14Δ cells, we induced cells that express the Spo15 protein fused to GFP to enter meiosis II and then stained them with Hoechst 33342 and the anti-Sad1 antibody. Spo15 is a SPB component that is required for SPB alteration in Meiosis II and sporulation (Ikemoto et al., 2000). The abnormal Sad1 signals colocalized with Spo15-GFP fluorescence signals (Fig. 3B). Thus, the organization or segregation of the SPBs in meu14Δ cells is abnormal. This suggests that the SPBs may not be able to act properly as scaffolds for forespore membrane formation, which may explain the lack of spore formation in meu14Δ cells. Supporting this is that the meu14Δ cells lack the crescent form of SPBs, which resembles the abnormality observed in spo15Δ cells (Ikemoto et al., 2000). Thus, the abnormal spore formation in meu14Δ cells may be due to a failure in the formation or segregation of SPBs during meiosis II.

Subcellular localization of Meu14-GFP during meiosis

To assess the behavior of the endogenous Meu14 protein during meiosis, we constructed a strain in which meu14$^+$ was replaced by a meu14$^+$-gfp gene that is designed to express the Meu14 protein fused with GFP at its C-terminal end. Since expression of this meu14$^+$-gfp gene is controlled by the native meu14$^+$ promoter, its expression is expected to be identical to that of the intact meu14$^+$ gene. That the meu14$^+$-gfp gene could fully complement the meiotic defects in meu14Δ diploid cells, and that these cells generated normal ascospores implies that the Meu14-GFP protein retains its function (data not shown). Western blot analysis using cell lysates reveals that the expressed Meu14-GFP protein migrates at the expected size, indicating it is not degraded in vivo (Fig. 4A). Western blotting also showed it is expressed only during meiosis II (4 to 8 hours) (Fig. 4A).

Cells carrying meu14$^+$-gfp were induced to enter meiosis and were fixed before fluorescence analysis of DNA, Meu14-GFP, and tubulin. The timing of meiotic progression in the meu14$^+$-gfp cells was confirmed to be quite similar to that of wild-type cells (data not shown). Based on the number of nuclei and the morphology of the microtubules, we judged the stage of meiosis of the individual cells and collected typical images to represent each stage of meiosis. Fluorescence signals from Meu14-GFP were not detected in mitotically growing cells or in early meiotic cells (at interphase, horse-tail, or meiosis I; Fig. 4B). The Meu14-GFP signal first appeared at prometaphase II as a blur in both the nucleus and the cytoplasm. After this, four strong rings appeared in the cells at metaphase II, and these four rings became bigger at anaphase II. The rings shrank at post-anaphase II and were again visualized as four small rings.

When we measured the distances between the two Meu14-GFP rings and plotted these versus the nuclear distance (Fig. 4C; upper right panel) or the length of microtubules (lower right panel), we found that the curves are similar, indicating that the Meu14-GFP rings behave in good coordination with both nuclear division and microtubule elongation. By counting the number of cells displaying Meu14-GFP signals, we found that Meu14-GFP was detectable in 78% of short-spindle cells at prometaphase II, in 100% of elongated-spindle cells at anaphase II, and in 48% of spindle-negative cells at post-anaphase II.

Immunostaining at various stages of meiosis also revealed that Meu14-GFP localizes next to the Sad1 signal on the SPB only at metaphase II (Fig. 4D; white arrow). This suggests that Meu14-GFP is located on the cytoplasmic side of the SPB. When the nuclear pore complex (NPC) was immunostained with the mAB414 antibody (Wilkinson et al., 2000), Meu14-GFP was detected outside of the NPC at late meiosis II (Fig. 4E).

Localization of Meu14-GFP in live cells during meiosis

The behavior of Meu14-GFP during meiosis suggests that it is transiently expressed and then degraded (Fig. 1B, Fig. 4A), and that before its degradation it moves around in the cell. To further investigate this dynamic behavior of Meu14-GFP, we observed the protein in live meu14$^+$-gfp cells that were induced to enter meiosis and then stained with Hoechst 33342 to visualize the nucleus. The images have been stored as a file that can be run as an animation

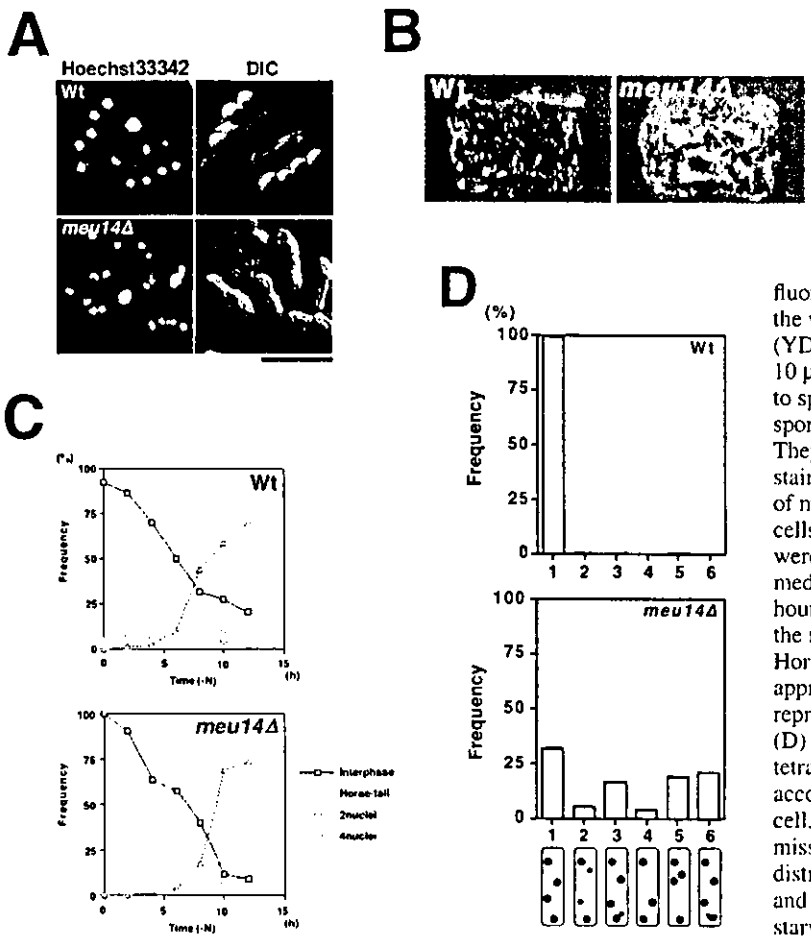

Fig. 2. Phenotypes of *meu14Δ* cells. (A) The *meu14* disruptant is defective in spore formation. Shown are DIC (differential interference contrast) and fluorescence photographs of Hoechst 33342-stained cells of the wild-type (TP4D-5A/TP4D-1D) and the *meu14Δ* mutant (YDO100) strains after 16 hours of nitrogen starvation. Bar, 10 μm. (B) Absence of spore walls in *meu14Δ* cells induced to sporulate. Wt and *meu14Δ* cells were streaked on a sporulation plate (EMM-N) and incubated at 28°C for 4 days. They were then exposed for 5 minutes to iodine vapor, which stains cells that have sporulated dark brown. (C) Progression of meiosis in wild-type and *meu14Δ* cells. Up to 1×10^7 cells/ml cultured overnight in liquid growth medium (EMM2) were incubated with shaking at 30°C in liquid sporulation medium (EMM-N). A portion of the culture was taken every 2 hours and stained with DAPI. Cells were classified based on the numbers of nuclei. □, interphase (mononucleate); ◇, Horse-tail; ○, binucleate; △, tetranucleate. For each sample, approximately 200 cells were counted. Values depict one representative result of four independent experiments. (D) The *meu14Δ* cells frequently produce abnormal tetranucleate cells. Tetranucleate cells were classified according to the number and position of the four nuclei per cell. 1, normal pattern; 2, unequally segregated nuclei; 3, missegregated nuclei; 4, unsegregated nuclei; 5, abnormally distributed nuclei; 6, distorted nuclei. The percentages of Wt and *meu14Δ* cells in each category after 12 hours of nitrogen starvation were compared. At least 200 cells were counted.

available on the internet. We show in Fig. 5 several time lapse images taken at 6 minute intervals of a cell passing from prophase II to metaphase II (Fig. 5A; see Movies 1 and 2, http://jcs.biologists.org/supplemental) and of a cell progressing from metaphase II to anaphase II (Fig. 5B; see Movies 3 and 4).

Meu14-GFP first appears at early meiosis II as a dot at the periphery of each of the two nuclei. The dots then duplicate and move around the nuclear membrane (as indicated by white arrowheads in Fig. 5Ai,ii). This behavior of Meu14-GFP resembles that of the SPB. Thereafter, the Meu14-GFP signals start to increase (time 0 in Fig. 5A) from the opposite ends of the two nuclei. Each nucleus develops small ring-shaped structures at either end. These structures gradually increase their diameters in a synchronized manner. The two rings approach each other until their diameters are maximized, after which they start to separate because of the nuclear division of meiosis II. Subsequently, as the nuclei separate from each other, the diameters of the two rings gradually shrink until they become two dots in the center of the two dividing nuclei (Fig. 5B). In post-anaphase II, the strengths of the Meu14-GFP ring/dot signals gradually diminish and the Meu14-GFP signal is observed to be diffusely distributed among the four spores. The diminished Meu14-GFP signal just before the maturation of the ascospores coincides with the disappearance of the Meu14-GFP band in immunoblotting (Fig. 4A).

At the late stage of meiosis II, the dim stain throughout the nuclear region almost completely disappears and only rings are observed, which is shown in Fig. 5Aii and Fig. 5Bii. The pictures are colorless so as to highlight the GFP signals. These pictures suggest that Meu14 localizes in the nuclear region and then assembles into rings during meiosis II.

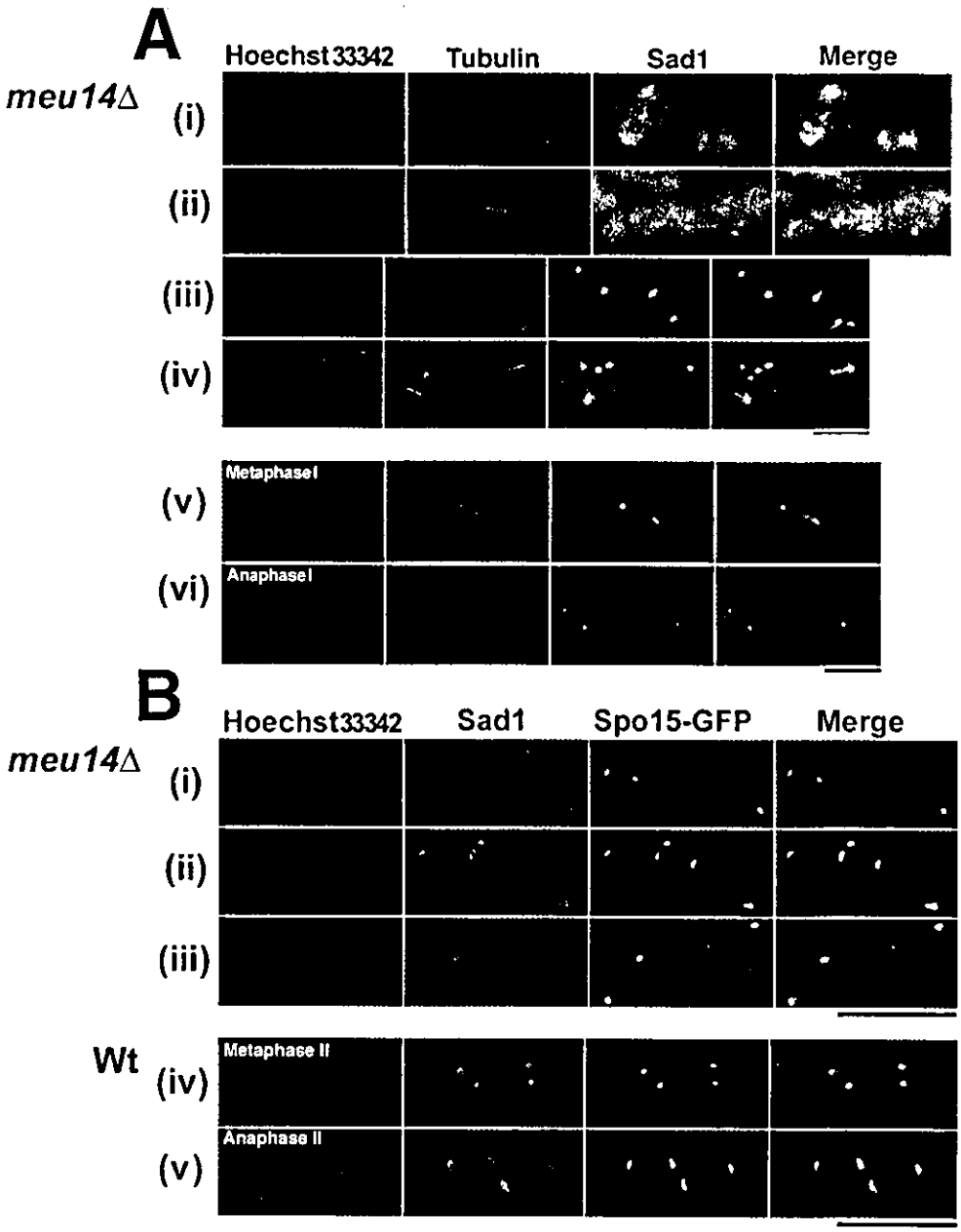

Fig. 3. Meu14 is required for the proper segregation of SPBs. (A) Chromosomal DNA, SPBs, microtubules in *meu14Δ* (YDO100) cells were stained by Hoechst 33342 (blue), anti-Sad1 antibody (green) and anti-α-tubulin antibody TAT-1 (red), respectively. Merged images are also shown. The following typical images are displayed. (i) Microtubule extension between the two pairs of dividing nuclei at meiosis II is not synchronized. (ii) Multiple foci of Sad1 staining are observed. (iii) Microtubules between the two nuclei are not detected. (iv) Localization of microtubules is abnormal and there are more than four Sad1 foci. (v,vi) *meu14Δ* (YDO100) cells at metaphase I (v) or anaphase I (vi). (B) Sad1 colocalizes with the SPB protein Spo15 during meiosis II. The following typical images are displayed for *meu14Δ* (YDO111) (i-iii) or wild-type (iv,v) cells. (i) One of the four SPBs is abnormal. (ii) More than four SPBs are observed. (iii) Nuclei are not properly divided at meiosis II. (iv,v) Wild-type cells at metaphase II (iv) and anaphase II (v). Bar, 10 μm.

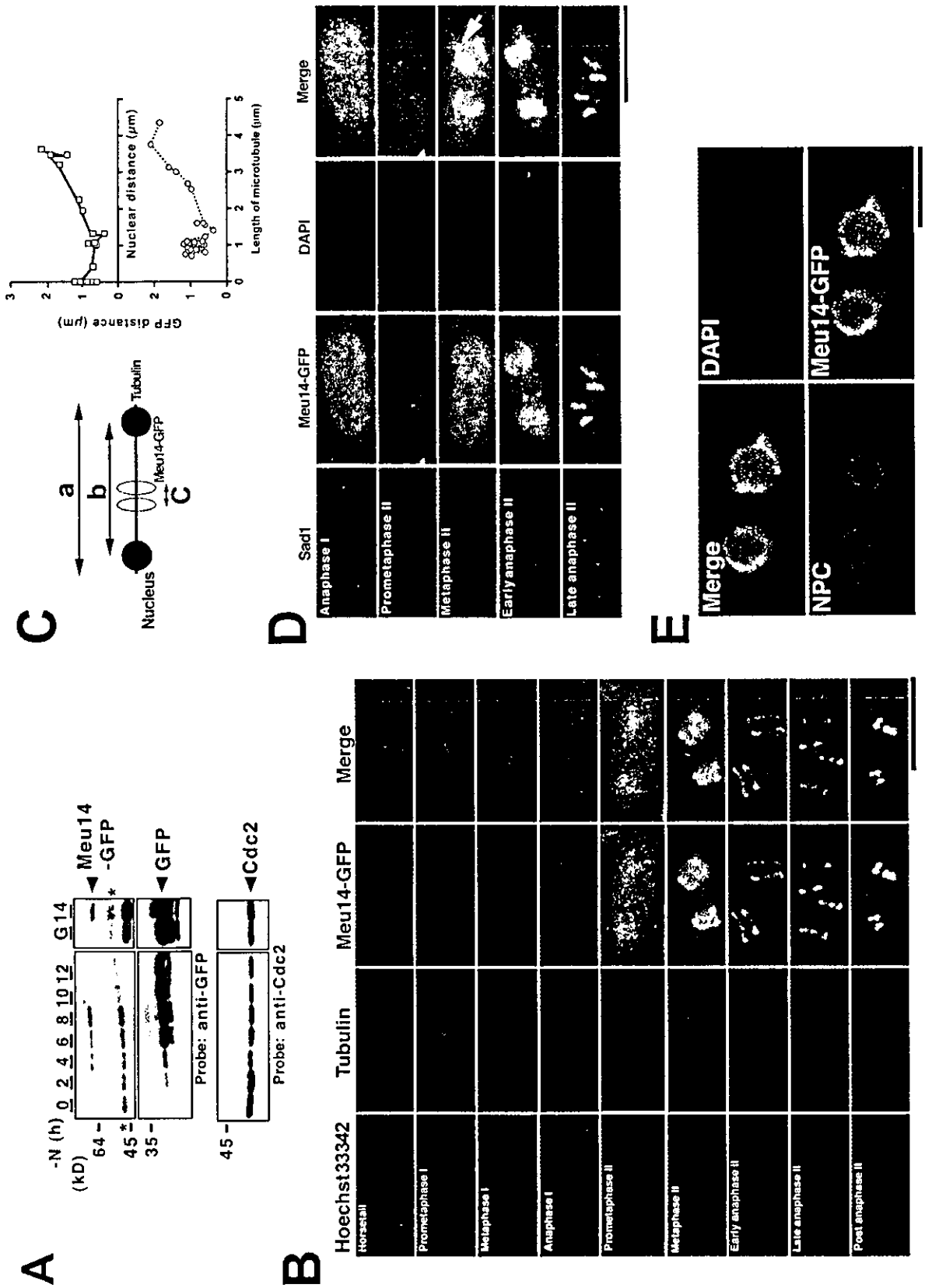
A
-N (h) 0 2 4 6 8 10 12 G14
(kD)
64
45
35
Meu14 -GFP
GFP
Probe: anti-GFP
45
Cdc2
Probe: anti-Cdc2
B
Hoechst33342
Tubulin
Meu14-GFP
Merge
Horsetail
Prometaphase I
Metaphase I
Anaphase I
Prometaphase II
Metaphase II
Early anaphase II
Late anaphase II
Post anaphase II
C
a
b
c
Tubulin
Meu14-GFP
Nucleus
GFP distance (μm)
Nuclear distance (μm)
Length of microtubule (μm)
D
Sad1
Meu14-GFP
DAPI
Merge
Anaphase I
Prometaphase II
Metaphase II
Early anaphase II
Late anaphase II
E
Merge
DAPI
NPC
Meu14-GFP